Article:

Bestenlehner, J.M. orcid.org/0000-0002-0859-5139, Crowther, P.A. orcid.org/0000-0001-6000-6920, Bronner, V.A. orcid.org/0000-0002-7624-2933 et al. (8 more authors) (2025) Binarity at LOw Metallicity (BLOeM): pipeline-determined physical properties of OB stars. Monthly Notices of the Royal Astronomical Society, 540 (4). pp. 3523-3548. ISSN 0035-8711

https://doi.org/10.1093/mnras/staf900

Monthly Notices of the ROYAL ASTRONOMICAL SOCIETY

MNRAS **540,** 3523–3548 (2025)
Advance Access publication 2025 June 3
https://doi.org/10.1093/mnras/staf900

Binarity at LOw Metallicity (BLOeM): pipeline-determined physical properties of OB stars

J. M. Bestenlehner [1,2] Paul A. Crowther [1]★ V. A. Bronner [3,4] S. Simón-Díaz,[5,6] D. J. Lennon,[5,6] J. Bodensteiner,[7,8] N. Langer,[9] P. Marchant [10,11] H. Sana,[10] F. R. N. Schneider [3,12] and T. Shenar [13]

[1]Astrophysics Research Cluster, School of Mathematical and Physical Sciences, University of Sheffield, Hicks Building, Hounsfield Road, Sheffield S3 7RH, UK
[2]School of Chemical, Materials and Biological Engineering, University of Sheffield, Sir Robert Hadfield Building, Mappin Street, Sheffield S1 3JD, UK
[3]Heidelberg Institute for Theoretical Studies, Schloss-Wolfsbrunnenweg 35, 69118 Heidelberg, Germany
[4]Department of Physics & Astronomy, Universität Heidelberg, Im Nuenheimer Feld 226, 69120 Heidelberg, Germany
[5]Instituto de Astrofísica de Canarias, Calle viá Láctea, s/n, 38205 La Laguna, Santa Cruz de Tenerife, Spain
[6]Departamento de Astrofísica, Universidad de La Laguna, E-38205 La Laguna, Tenerife, Spain
[7]European Southern Observatory, Karl-Schwarzschild-Strasse 2, 85748 Garching bei München, Germany
[8]Anton Pannekoek Institute of Astronomy, University of Amsterdam, Postbus 94249, 1090 GE Amsterdam, Netherlands
[9]Argelander-Institut für Astronomie, Universität Bonn, Auf dem Hügel 71, 53121 Bonn, Germany
[10]Institute of Astronomy, KU Leuven, Celestijnenlaan 200D, B-3001 Leuven, Belgium
[11]Sterrenkundig Observatorium, Universiteit Gent, Krijgslaan 281 S9, B-9000 Gent, Belgium
[12]Astronomisches Rechen-Institut, Zentrum für Astronomie der Universität Heidelberg, Mönchhofstr. 12-14, 69120 Heidelberg, Germany
[13]School of Physics and Astronomy, Tel Aviv University, Tel Aviv 6997801, Israel

Accepted 2025 May 23. Received 2025 May 20; in original form 2025 March 7

ABSTRACT

We aim to determine the physical properties of OB stars from the multi-epoch Binarity at LOw Metallicity (BLOeM) spectroscopic survey of the Small Magellanic Cloud using the Very Large Telescope/Fibre Large Array Multi-Element Spectrograph. We apply a pipeline designed to analyse large spectroscopic samples of OB stars to the co-added, initial nine epochs of the BLOeM survey, utilizing grids of synthetic model spectra computed with the stellar atmosphere code FASTWIND. 69 OB stars are excluded from the analysis owing to disc emission or significant contamination by secondaries in SB2 binaries. We determine physical properties of 778 OB stars, including $T_{\rm eff}$, $\log g$, $\log L/{\rm L}_{\odot}$, and $v_{\rm e}\sin i$. There appears to be a bimodality in $v_{\rm e}\sin i$ of single O stars, while $v_{\rm e}\sin i$ distributions of OB stars are strikingly different for single (median 78 km s^{-1}) and binary (median 200 km s^{-1}) systems. Inferred temperatures are broadly in agreement with literature results for stars in common, plus results from a grid-based automization tool for a subset of O and early B stars, although uncertainties are larger for surface gravities. Rotational velocities are broadly in line with an independent tool applied to the same subset. We recover the anticipated lower mass cut-off at 8 M$_{\odot}$ from the survey design using a Bayesian inference method coupled with SMC metallicity evolutionary models, with median masses of 12.6 M$_{\odot}$ (19.8 M$_{\odot}$) for B-type (O-type) stars. Spectroscopic masses exceed evolutionary masses, albeit with large uncertainties in surface gravities. We also provide an updated catalogue of O stars in the SMC since half of the 159 BLOeM O stars are newly classified as O-type stars.

Key words: stars: atmospheres – stars: early-type – stars: fundamental parameters – stars: massive – stars: rotation.

1 INTRODUCTION

Massive stars ($M_{\rm init} \geq 8$ M$_{\odot}$), despite their rarity, are major contributors to the radiative, chemical, and mechanical feedback of star-forming galaxies, owing to their high temperatures, production of α-elements, and powerful stellar winds (Geen et al. 2023). They are responsible for core-collapse supernovae (Smartt 2015), gamma-ray bursts (Gehrels, Ramirez-Ruiz & Fox 2009) and compact objects responsible for gravitational waves (Abbott et al. 2016), especially at low metallicity.

Massive stars in the Milky Way are overwhelmingly found in close binaries (Sana et al. 2012), affecting the evolution of the system (de Mink et al. 2014), and consequently the lifetime, feedback, and ultimate fate of each component. Large spectroscopic surveys of massive stars in the Large Magellanic Cloud (LMC), with a present-day metallicity of 1/2 Z$_{\odot}$, also reveal a high close binary fraction amongst massive stars (Sana et al. 2013).

The proximity of the Small Magellanic Cloud (SMC), with a present-day metallicity of 1/5 Z$_{\odot}$ (Russell & Dopita 1990), provides our best view of individual metal-poor massive stars. Binarity at LOw Metallicity (BLOeM; Shenar et al. 2024) involves a multi-epoch spectroscopic survey of 929 massive stars in the SMC using the Fibre Large Array Multi-Element Spectrograph (FLAMES, Pasquini et al. 2002) at the Very Large Telescope (VLT). The selection

★ E-mail: paul.crowther@sheffield.ac.uk

criteria for BLOeM targets focused on bright, blue sources from the Gaia DR3 catalogue (see fig. 2 of Shenar et al. 2024), to ensure targets were representative of massive stars in the SMC. The use of a fibre-fed instrument (FLAMES) hindered sampling of crowded environments, such as the NGC 346 star-forming region (Massey, Parker & Garmany 1989; Dufton et al. 2019; Rickard et al. 2022). Early results also favour a high close binary fraction of O and B-type stars (Sana et al. 2025; Villaseñor et al. 2025).

Multiple systems in tight orbits range from double-lined (SB2) spectroscopic binaries in which both components contribute significantly at optical wavelengths, to single-lined (SB1) systems in which one component dominates, owing to a faint stellar or compact companion. Techniques used to analyse SB2 systems include spectral disentangling (Mahy et al. 2020), which can also be used for SB1 systems to detect or rule out faint stellar companions (Shenar et al. 2022). In all cases, it is necessary to determine stellar parameters for OB stars, which is generally resource intensive. Spectral analysis of metal poor B stars is especially challenging since metal lines, which serve as primary temperature diagnostics (e.g. Becker & Butler 1990), are much weaker than for Milky Way counterparts (Walborn 1983).

In contrast to late-type stars, spectroscopic studies of hot, luminous stars usually involve one of two approaches. Coarse physical parameters can be estimated from spectral type-temperature calibrations, as was undertaken by Shenar et al. (2024) for the BLOeM sample. Alternatively, detailed analysis of individual stars can be undertaken, owing to the large parameter space involved and requirement to use sophisticated non-LTE model atmospheres. Studies of very large samples typically involve a grid-based star-by-star approach (Castro et al. 2018; Holgado et al. 2018; Ramachandran et al. 2019). Here, we exploit a new pipeline for the efficient analysis of very large samples of optical OB spectra (Bestenlehner et al. 2024). This study of the entire BLOeM OB sample will be complemented by bespoke studies of sub-samples, and upcoming studies focused on specific quantities such as rotational velocities (Berlanas et al., in preparation).

We present BLOeM data sets in Section 2 and briefly describe the pipeline used to analyse OB stars in Section 3. We present our derived physical parameters in Section 4, including comparisons with previous results. Section 5 discusses rotational velocities, while Section 6 presents tailored analyses of a subset of BLOeM stars using the grid-based *interactive* tool IACOB-GBAT (Simón-Díaz et al. 2011) for comparison with pipeline results. Spectroscopic masses are compared to evolutionary mass determinations in Section 7, followed by a consideration of the BLOeM O star sample within the context of the global SMC population in Section 8. Finally, brief conclusions are drawn in Section 9. Appendices include pipeline results, comparisons with previous studies and an updated catalogue of O stars in the SMC, since there have been many discoveries since the census of Bonanos et al. (2010).

2 BLOEM OBSERVATIONS

The BLOeM survey (PI: Shenar, Co-PI: Bodensteiner) involves 25 epoch spectroscopy of 929 massive stars with FLAMES at the VLT, using the LR02 setup ($\lambda\lambda$3950–4550Å, $R = 6200$) between October 2023 and late 2025. Targets were drawn from a *Gaia* catalogue of bright, blue stars, which peaks at $G \sim 14.6$ mag, and has a limiting magnitude of $G = 16.5$ mag, as shown in fig. 2 of Shenar et al. (2024). The use of eight FLAMES fields allowed a reasonable fraction of the SMC to be considered, albeit with limited sampling of young, luminous stars in rich star-forming regions (e.g. Evans et al. 2006; Dufton et al. 2019). The data reduction process is described in Shenar et al. (2024).

For the present study the first nine epochs (2023 Oct–2023 Dec) are considered, with individual spectroscopic data sets obtained by co-adding two normalized back-to-back 615 sec exposures. Average radial velocities, $v_{\rm rad}$, and dispersions, $\sigma(v_{\rm rad})$ are obtained for all OB stars and presented in Table A1 (see supplementary data) with the exception of stars exhibiting unusual spectral features (e.g. B[e] supergiants).

The primary purpose of multi-epoch spectroscopy is to investigate the multiplicity of massive stars at low metallicity. Binarity is assessed via peak-to-peak radial velocities of $\geq$20 km s^{-1} at the 4σ significance level, with the initial nine epoch data set split into five studies, focused on O stars (Sana et al. 2025), OBe stars (Bodensteiner et al. 2025), non-supergiant early B stars (Villaseñor et al. 2025), early B supergiants (Britavskiy et al. 2025) and cooler supergiants (Patrick et al. 2025). Short period spectroscopic binaries (some of which may be higher order systems) from these studies are indicated in Table A1 (see supplementary data) and include supergiants for which variability arises either from a companion (SB1) or intrinsic line profile variability (lpv). The true multiplicity fraction of BLOeM stars is doubtless higher, such that stars categorized as 'single' are preliminary, with definitive results awaiting analysis of the complete 25 epoch data set.

Shenar et al. (2024) also describes cross-correlation and co-addition of individual normalized observations to improve signal-to-noise ratio for classification and quantitative analysis. This is the primary data set used in the present study. The LR02 setup includes the majority of diagnostics necessary for quantitative studies of OB stars, including multiple He I-II lines for the determination of temperatures for O and early B stars, plus N IV λ4058 for early O stars. Si IV $\lambda\lambda$4089–4116, Si III λ4553, Si II $\lambda\lambda$4128–31 and Mg II λ4481 are available for B stars lacking He II diagnostics, together with multiple He I lines. Hγ and Hδ permit surface gravities to be determined, noting Hϵ lies at the edge of the LR02 spectral coverage. Hα and He II λ4686 are excluded, so it is not possible to determine wind properties from the current BLOeM observations.

The grid used in our spectroscopic pipeline is suitable for the determination of physical parameters of OB stars, so 81 AF supergiants are excluded. Their physical parameters are considered by Patrick et al. (2025). In addition, the subset of SB2 systems in which both components are prominent in the co-added data sets are also excluded, as are OB stars in which the Balmer (and sometimes He I) lines exhibit strong emission components, i.e. OBe stars and OB stars within regions of strong nebulosity (e.g. NGC 346, Evans et al. 2006). We also exclude B[e] supergiants from our analysis.

In total we present analyses of 778 OB stars, representing 84 per cent of the BLOeM sample of 929 stars, or 92 per cent of the 847 OB stars. Confirmed or suspected spectroscopic binaries (SB1, SB2, SB3) are indicated in Table A1 and represent 42 per cent (329 stars) of the total sample studied. A breakdown of OB statistics from BLOeM (Shenar et al. 2024) and the present study is provided in Table 1.

3 SPECTROSCOPIC PIPELINE

For our spectroscopic analysis pipeline, we employ grids of synthetic model spectra computed with v10.6 of the non-LTE atmosphere code FASTWIND (Puls et al. 2005; Rivero González et al. 2012) including H, He, C, N, O, Si, and Mg as explicit elements at the SMC metallicity (0.2 $Z_{\odot}$). Grids covered the following parameter space log $T_{\rm eff}$ (K) over [4.0, 4.775] in 0.025 dex steps, corresponding to 10 kK $\leq T_{\rm eff} \leq$ 60 kK, log g (cm s^{-2}) over [1.5, 4.5] in 0.2 dex steps, and Helium abundances in mass-fraction Y over [0.15, 0.55]

Table 1. Breakdown of 847 OB stars identified in the BLOeM survey (Shenar et al. 2024) by spectral type and single versus multiple, according to analysis of the initial nine epoch data set (Bodensteiner et al. 2025; Britavskiy et al. 2025; Patrick et al. 2025; Sana et al. 2025; Villaseñor et al. 2025). Sources excluded from the present study (69 sources) include a subset of SB2 binaries, OBe stars plus a few OB stars contaminated by strong nebular emission. Miscellaneous targets excluded from analysis are B[e] supergiants (BLOeM 2-116, 3-012, 4-055), sources with B + A composite appearance (BLOeM 3-006, 8-009, 8-056) and two B9 supergiants (BLOeM 5-036, 5-086) for which fits were unsatisfactory.

Spectral type	– Included – Single	Multiple	– Excluded – Single	Multiple	Misc.	Total
O-type	71	66	14	8	0	159
B-type	380	261	32	7	8	688
Total	451	327	46	15	8	847

in 0.05 steps. Convergence difficulties were experienced at the lowest temperatures ($T_{\rm eff} \leq 15$ kK) impacting on fits to late B supergiants.

Although the FLAMES LR02 setup excludes typical wind diagnostics, the wind-strength parameter $\log Q$ was retained as a variable, ranging from -11.4 to -15.0 in 0.3 dex steps, where $Q = \dot{M}(R_* v_\infty)^{-3/2}$ with units $\mathrm{M_\odot\,yr^{-1}}$, $\mathrm{R_\odot}$, and $\mathrm{km\,s^{-1}}$. A smooth wind with volume filling factor $f_{\rm v} = 1$ and $\beta = 1$ velocity law was assumed and the micro-turbulent velocity was set to $v_{\rm mic} = 10\,\mathrm{km\,s^{-1}}$ in the model grids.

Typical macro-turbulent velocities for OB stars are in the range between a few $\mathrm{km\,s^{-1}}$ to several tens of $\mathrm{km\,s^{-1}}$, although can reach higher values (Simón-Díaz et al. 2017). The velocity resolution of the LR02 FLAMES data set is $48\,\mathrm{km\,s^{-1}}$. We convolved our synthetic grid with a fixed $v_{\rm mac} = 20\,\mathrm{km\,s^{-1}}$ and assumed any additional broadening is due to rotation, with projected rotational velocities of $v_{\rm e} \sin i$ = [0, 10, 20, 35, 50, 75, 100, 150, 200, 250, 300, 350, 400, 450, 500] $\mathrm{km\,s^{-1}}$.

A complete description of the pipeline[1] is provided in Bestenlehner et al. (2024). In brief, we used the full FLAMES spectral range including the observational error spectrum by utilizing a χ^2 minimization Ansatz:

$$\chi^2 = (\boldsymbol{d} - \mathbf{R}\boldsymbol{s})^{\rm T}\mathbf{N}^{-1}(\boldsymbol{d} - \mathbf{R}\boldsymbol{s}) \quad (1)$$

with $\boldsymbol{d}$ the observed and $\boldsymbol{s}$ the synthetic spectra, $\mathbf{R}$ the instrumental responds matrix and observational, diagonal error matrix $\mathbf{N}$. As model uncertainties should be budgeted into the parameter determination, we 'de-idealized' the model spectrum $\boldsymbol{s}$ according to Bestenlehner et al. (2024).

Our sample is fairly heterogeneous, ranging from early O dwarfs to late B supergiants, albeit with a large number of early B stars. Therefore, the model-error is averaged over the entire parameter space of our sample. This impacted the overall performance of the pipeline, because a meaningful model-error should ideally be based on a sample of similar objects (c.f. the discussion in Bestenlehner et al. 2024).

The combined BLOeM data sets are cross-correlated with synthetic spectral templates to determine a mean radial velocity ($v_{\rm rad}$), and then corrected for this shift before being sampled on the wavelength grid of the synthetic spectra. Fig. 1 shows radial velocities of single OB stars with respect to the $+183\,\mathrm{km\,s^{-1}}$ mean value of the BLOeM sample. For comparison, Hilditch, Howarth & Harries (2005) obtained mean systemic velocities of $+196\,\mathrm{km\,s^{-1}}$ for OB eclipsing binaries in the SMC while Evans & Howarth (2008) obtained a mean of $+172.0\,\mathrm{km\,s^{-1}}$ for the 2dFS sample and highlighted differences between the bar ($+167.4\,\mathrm{km\,s^{-1}}$) and the wing ($+189.5\,\mathrm{km\,s^{-1}}$) which are also apparent in Fig. 1.

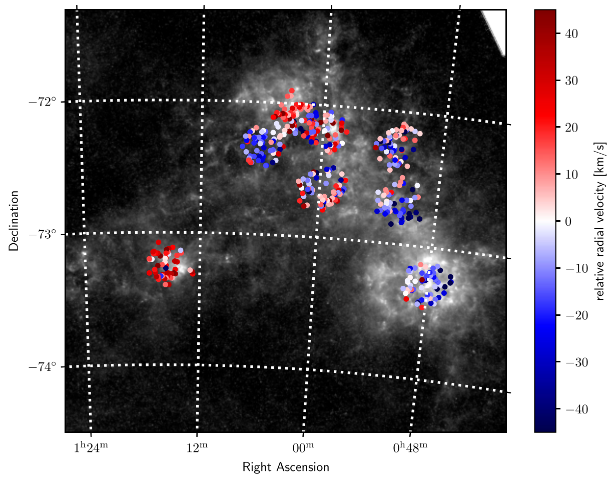

Figure 1. Radial velocities of single BLOeM OB stars – according to initial nine epoch data set – relative to $183\,\mathrm{km\,s^{-1}}$ average of sample, overlaid on a *Herschel* SPIRE 350 μm map of the SMC (Meixner et al. 2013). Higher radial velocities for OB stars in the wing (south east) has previously been reported by Evans & Howarth (2008).

Hydrogen lines are the most prominent spectroscopic features in the blue spectra of OB stars and dominate the χ^2, with He lines sometimes as weak as metal lines. First, we initialize a wavelength array with 0.1Å spacing around the spectral lines in our FASTWIND LINES-list. Secondly, we increased the number of wavelength points by a factor of 5 beyond ±5Å of the central wavelength of the Balmer lines, because $\log g$ is based on the pressure-broadened wings. Thirdly, we increased the number of wavelength points by a factor of 25 within ±1Å of the central wavelength of the Helium and metal lines.

Our default approach is not to increase the weighting of any specific spectral features for those samples involving a broad range of spectral types, such as BLOeM. However, weak Si IV λλ4089, 4116 features were poorly reproduced for a large subset of early B stars, leading to an unphysical gap in solutions close to $T_{\rm eff} \sim 25$ kK.

Increased weight for both Si IV lines improved temperatures to the detriment of surface gravities (both lie within the wing of H δ) so we ultimately elected to adopt an increased weighting of solely Si IV λ4089. The higher weighing of λ4089 generally led to improved fits, without adversely affecting surface gravities. This was achieved by incorporating more data points around this line (4088.85±0.25Å).

O II λ4089.29 (Wenåker 1990) was not included in the FASTWIND line list for spectral line synthesis, but contributes to the Si IV λ4089 feature in early B stars (see Hardorp & Scholz 1970; Becker & Butler 1988; Kilian, Montenbruck & Nissen 1991; de Burgos et al. 2024). However, the pipeline is designed to handle model deficiencies such as missing spectral lines or inaccurate physics (see Bestenlehner et al. 2024, Section 2).

Test calculations incorporating O II λ4089[2] have been undertaken for FASTWIND models at $\log g/(\mathrm{cm\,s^{-2}}) = 3.3$ for $T_{\rm eff} = 30$, 25, and 20 kK, indicating that O II λ4089 is a minor, major, and primary contributor to the blend, respectively. At $T_{\rm eff} = 25$ kK the addition of

[1] https://github.com/jbestenlehner/mdi_analysis_pipeline

[2] O II oscillator strengths were obtained from the Vienna Atomic Line Data base (VALD), which compare closely to R-Matrix calculations from Becker & Butler (1988).

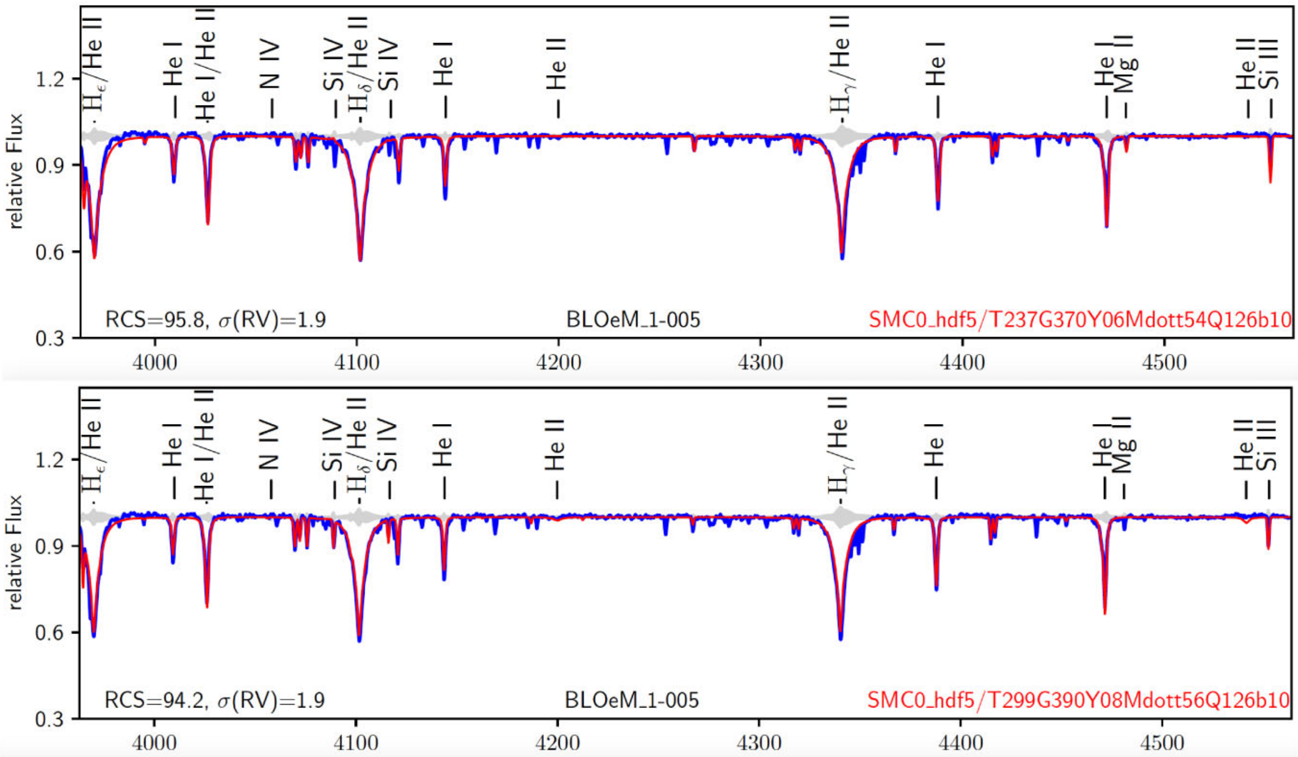

Figure 2. Comparison between the pipeline fits (red) obtained for BLOeM 1-005 (B1 II, blue) for the unweighted solution [upper panel, $T_{\mathrm{eff}} = 23.6^{+0.7}_{-0.8}$ kK, $\log g/(\mathrm{cm\,s^{-2}}) = 3.64^{+0.15}_{-0.16}$] versus the solution with additional weight given to Si IV λ4089 [lower panel, $T_{\mathrm{eff}} = 29.9 \pm 1.2$ kK, $\log g/(\mathrm{cm\,s^{-2}}) = 3.93^{+0.34}_{-0.17}$]. It is apparent that both solutions reproduce H I and He I lines plus Si III λ4553, with the higher temperature solution matching Si IV $\lambda\lambda$4089–4116 and the lower temperature solution reproducing Mg II λ4481. The grey shaded area is the square root of the diagonal elements of the model-error uncertainty matrix calculated by the pipeline. RCS refers to the reduced χ^2 and σ(RV) refers to the dispersion in radial velocities.

O II would significantly boost the strength of the λ4089 feature, and so would impact on the favoured solution. At $T_{\mathrm{eff}} = 30$ kK several other high ionization lines (e.g. He II) are present, so the contribution from O II is not anticipated to adversely impact the favoured solution. At $T_{\mathrm{eff}} = 20$ kK, the blend is weak, with primarily Si III and Mg II observed, so again the solution is not anticipated to be impacted by the omission of O II λ4089.

We have also considered an alternate increased weighting of Si IV λ4116, the weaker component of the doublet, but ultimately favoured λ4089 owing to its greater strength in early B stars. To reiterate, many spectral lines contributed to the pipeline fit (including Si IV λ4116), in contrast to usual practice which focus *solely* on Si lines in early B stars (e.g. Dufton et al. 2018), albeit with additional weighting to Si IV λ4089 that produced more robust solutions.

By way of example, Fig. 2 illustrates unweighted (upper panel) and weighted (lower panel) solutions (red) for BLOeM 1-005 (B1 II, blue) for which $T_{\mathrm{eff}} = 23.6^{+0.7}_{-0.6}$ kK, $\log g/(\mathrm{cm\,s^{-2}}) = 3.64^{+0.15}_{-0.16}$ and $T_{\mathrm{eff}} = 29.9 \pm 1.2$ kK, $\log g/(\mathrm{cm\,s^{-2}}) = 3.93^{+0.34}_{-0.17}$ are obtained, respectively. The unweighted solution reproduces most features (including Mg II λ4481) aside for Si IV λ4089–4116, with Si III λ4553 somewhat too strong. In contrast, the weighted solution addresses the mismatch to the Si IV $\lambda\lambda$4089–4116 doublet, and improves the match to Si III λ4553, albeit at the expense of Mg II λ4481. BLOeM 1-005 is representative of OB stars analysed in this study, since its *Gaia G*-band brightness (G = 14.6 mag) corresponds to the photometric peak of the BLOeM sample.

The stellar atmosphere grid is non-rectilinear since a subset of models did not converge or failed to compute due to unphysical parameter space (e.g. Eddington limit). Before determining the uncertainties we fill the gaps in the probability distribution function (PDF) with zero-values, so that the PDF becomes a 4D($T_{\mathrm{eff}} - \log g - \log Q - Y$) rectilinear grid. The 4D grid was then interpolated to artificially increase the grid resolution using the multidimensional interpolation function SCIPY.INTERPOLATE.INTERPN with cubic-spline method to obtain more accurate parameters and less grid-specific uncertainties.

We used the following standard deviations in 4D; 1σ: 0.0902, 2σ: 0.5940, and 3σ: 0.9389, following Wang, Shi & Miao (2015). CNO abundances and $v_e \sin i$ were not included as they mainly improve the fit to the nitrogen lines and the line broadening, but also a 6D grid interpolation becomes computationally very expensive. In a few instances, the 4D grid leads to multiple minima in which local minima with the lowest χ^2 solutions preferred. In the few instances for which $\Delta T/T_{\mathrm{eff}} > 10$ per cent, there are no significant differences between the fits obtained.

In order to determine bolometric luminosities, we adopted a distance modulus of 18.98 mag (Graczyk et al. 2020) for the SMC, and used optical (Gaia Collaboration 2021) and near-IR photometry for the determination of interstellar reddening. Note that K_s-band photometry presented in table A2 of Shenar et al. (2024) is a mixture of 2MASS (Skrutskie et al. 2006) and aperture photometry from VMC (Cioni et al. 2011) rather than PSF photometry of the latter survey. For the present study K_s-band photometry are utilized, either from VMC PSF photometry or 2MASS Point Source Catalogue if $m_{K_s} < 13.2$ mag (see Table A1).

Individual reddening parameters R_{5495} and $E_{4405-5495}$ were obtained by fitting individual photometric fluxes to the model spectral

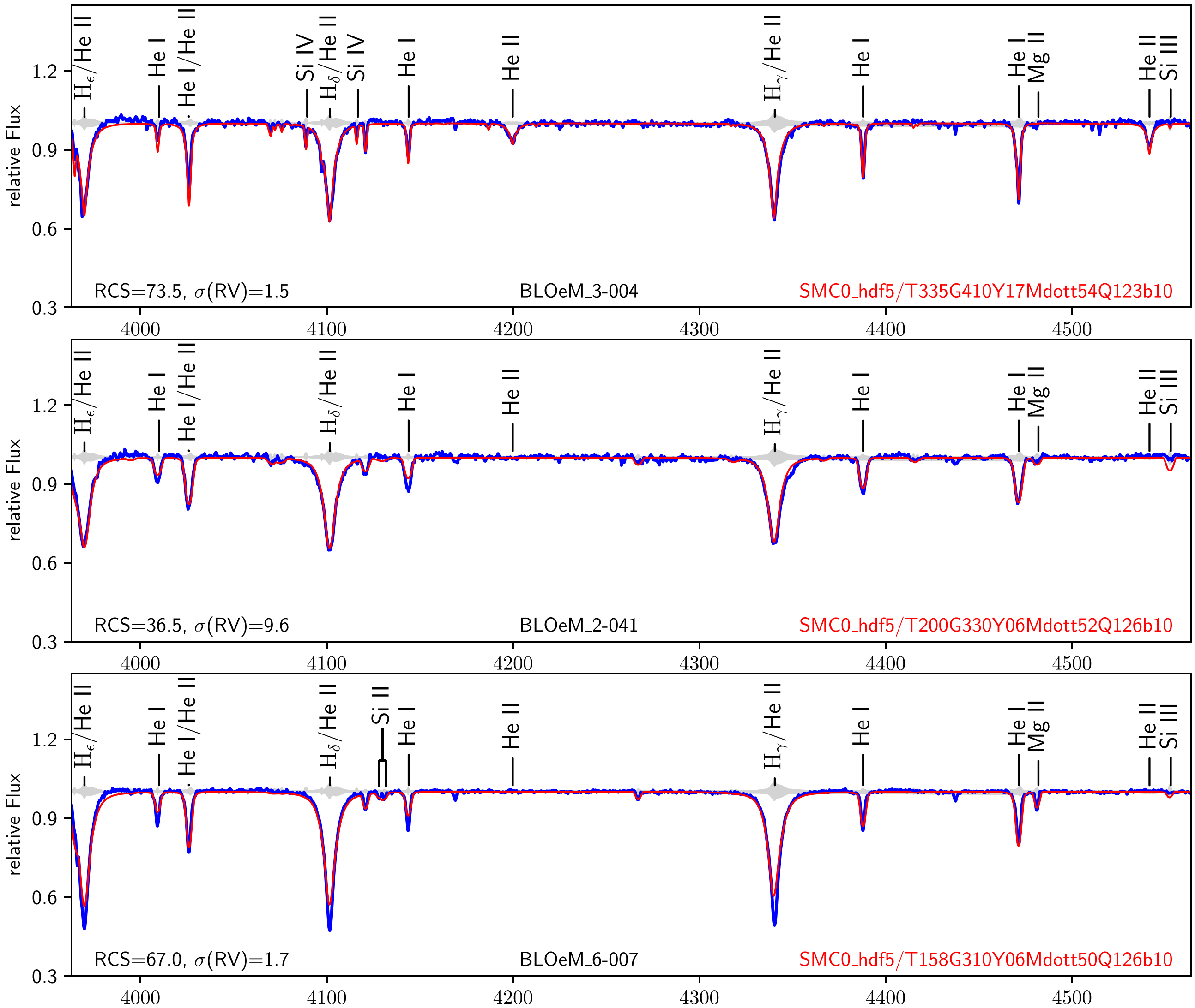

Figure 3. Comparison between the pipeline fits (red) obtained for visually faint OB stars, from top to bottom: BLOeM 3-004 (O9.7 IV:) for which $T_{\rm eff} = 33.7^{+1.5}_{-2.3}$ kK, $\log g$/cm s^{-2} = $4.12^{+0.34}_{-0.43}$, BLOeM 2-041 (B2: II), for which $T_{\rm eff} = 20.1^{+4.7}_{-2.7}$ kK, $\log g$/cm s^{-2} = $3.30^{+0.74}_{-0.40}$ and BLOeM 6-007 (B5 II), for which $T_{\rm eff} = 15.9 \pm 0.8$ kK, $\log g$/cm s^{-2} = $3.07^{+0.17}_{-0.29}$. The grey shaded area is the square root of the diagonal elements of the model-error uncertainty matrix calculated by the pipeline. RCS refers to the reduced χ^2 and σ(RV) refers to the dispersion in radial velocities.

energy distribution employing the reddening law of Maíz Apellániz et al. (2014). $R_{\rm V} = 3.0$ for the SMC bar has been determined by Gordon et al. (2024). Inferred interstellar extinctions are modest, with an average of $A_{5495} \simeq A_{\rm V} = 0.39 \pm 0.14$ mag, as expected for *Gaia* colour selected targets towards SMC sightlines, with individual values included in Table A1.

4 PHYSICAL PROPERTIES OF BLOEM OB STARS

Table A1 presents inferred physical parameters for 778 OB stars from BLOeM. For completeness, we include radial velocities (and dispersions) of all OB stars. Online material includes spectral fits for each star (model in red, observations in blue) at 10.5281/zenodo.15526149. 69 SB2 systems, OBe stars, OB stars with strong nebular emission and B[e] supergiants are excluded from our analysis.

By way of example, Fig. 3 presents the solution (model in red) for several visually faint OB stars, from top to bottom: BLOeM 3-004 (O9.7 IV:, $G = 16.0$ mag), BLOeM 2-041 (B2: II, $G = 16.2$ mag) and BLOeM 6-007 (B5 II, $G = 15.0$ mag). The overall fit quality to H I, He I-II, Si IV λ4088–4116, Si II λ4128–31, and Mg II λ4481 lines is satisfactory, although Si III λ4553 is over predicted in BLOeM 2-041, and the cores of strong He I and Balmer lines are under predicted in BLOeM 6-007.

4.1 Stellar temperatures

Fig. 4 compares BLOeM spectral types with pipeline-derived effective temperatures. Overall there is a clear correlation between spectral type and inferred temperature, although there is a large (unrealistic) spread in temperatures for stars close to B1. This spread is highlighted in Fig. 5, which compares $T_{\rm eff}$ adopted from calibrations in Shenar et al. (2024) with pipeline values. This issue arises despite the increased weighting to Si IV λ4089, with lower temperatures obtained if Si IV is not reproduced (recall Fig. 2).

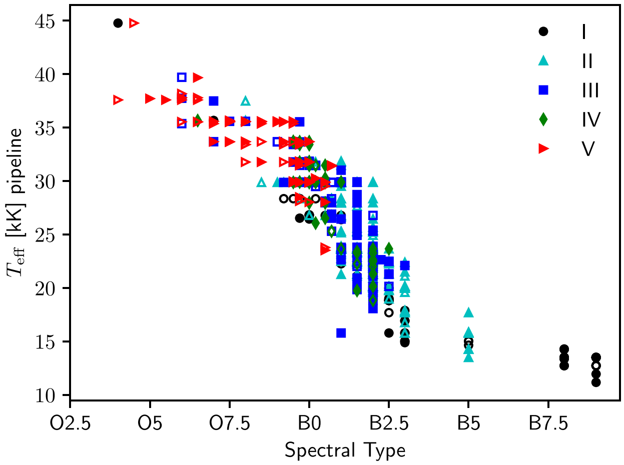

Figure 4. Pipeline effective temperatures, $T_{\rm eff}$ for BLOeM OB stars using spectral types from Shenar et al. (2024). Single stars according to analysis of the initial nine epochs of BLOeM (Bodensteiner et al. 2025; Britavskiy et al. 2025; Patrick et al. 2025; Sana et al. 2025; Villaseñor et al. 2025), are open symbols, multiples are filled symbols.

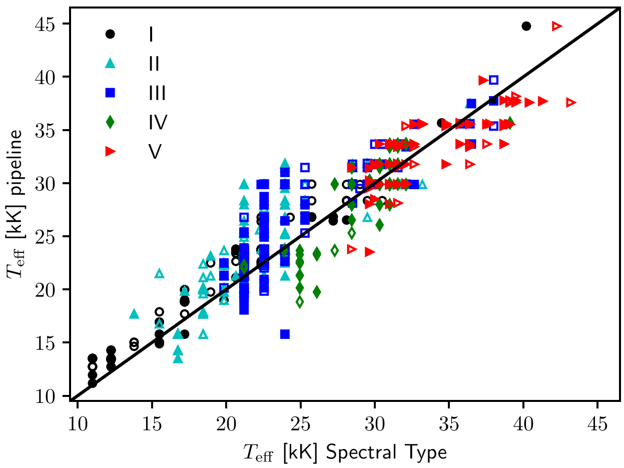

Figure 5. Comparison between adopted $T_{\rm eff}$ of BLOeM OB stars from SMC calibrations (Shenar et al. 2024) and pipeline-derived, $T_{\rm eff}$. Single stars according to analysis of the initial nine epochs of BLOeM (Bodensteiner et al. 2025; Britavskiy et al. 2025; Patrick et al. 2025; Sana et al. 2025; Villaseñor et al. 2025) are open symbols, multiples are filled symbols.

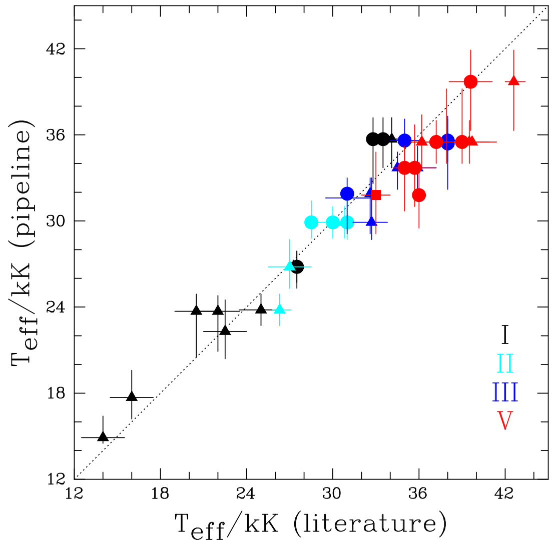

Figure 6. Comparison between $T_{\rm eff}$ for BLOeM OB stars from literature studies (circles: CMFGEN, triangles: FASTWIND, squares: TLUSTY) and the current pipeline, colour coded by luminosity class. References are provided in the Appendix in Tables B1 and B2.

A subset of the BLOeM stars have been subject to earlier quantitative spectral analysis efforts, primarily those in common with the ULLYSES/XShootU sample (Vink et al. 2023; Roman-Duval et al. 2025). We compare our derived temperatures to detailed literature results in the Appendix in Table B1 (B2) for O-type (B-type) stars. Previous studies utilized UV and optical spectroscopic data sets, plus either CMFGEN (Hillier & Miller 1998), FASTWIND (Puls et al. 2005; Rivero González et al. 2012), or TLUSTY (Hubeny & Lanz 1995).

Overall pipeline-derived temperatures agree reasonably well with detailed studies within the uncertainties, as illustrated for OB stars in Fig. 6, although large uncertainties are obtained in some instances (e.g. BLOeM 4-020, B0 Ib-Iab). For the BLOeM subset of late B stars, Patrick et al. (2025) have estimated temperatures from comparison with CMFGEN models. Pipeline temperatures are systematically warmer for B5 and B8 subtypes by 1.0 and 0.9 kK, respectively, increasing to 2.4 kK for B9 supergiants, arising from FASTWIND model convergence difficulties at the lowest temperatures (He I lines are generally overestimated).

In addition to previously detailed spectroscopic studies for BLOeM OB stars, Castro et al. (2018) have also determined temperatures of a large sample of SMC field OB stars from the RIOTS4 survey (Lamb et al. 2016) using a grid of FASTWIND models. Castro et al. (2018) relied solely on H and He diagnostics, so their temperatures will be less robust for B stars in which He II is not observed. 25 OB stars are in common between the present study and Castro et al. (2018), listed in the Appendix (Table C1), with log $T_{\rm eff}$ (pipeline)−log $T_{\rm eff}$(Castro) = +0.04±0.10 dex.

Bestenlehner et al. (2025) have also applied the pipeline described in Section 3 to XShootU data sets (Vink et al. 2023). 30 OB stars are in common between the present study and Bestenlehner et al. (2025), with parameters compared in the Appendix (Table D1). Our derived temperatures agree well with the XShootU pipeline analysis, with log $T_{\rm eff}$ (BLOeM)−log $T_{\rm eff}$(XShootU) = +0.00±0.02 dex, indicating that the lack of wind spectral diagnostics does not adversely impact stellar temperatures. We will revisit effective temperatures in Section 6.

4.2 Stellar luminosities

Fig. 7 presents pipeline results for OB stars in a Hertzsprung–Russell (HR) diagram, superimposed upon non-rotating SMC metallicity evolutionary tracks from Schootemeijer et al. (2019), for which semi-convection and overshooting parameters follow Brott et al. (2011). This represents a more robust HR diagram than that presented in Shenar et al. (2024) which was based upon spectral type calibrations.

The lack of O stars close to the theoretical zero age main sequence (ZAMS) is striking, in common with previous Milky Way (Holgado et al. 2020), LMC (Sabín-Sanjulián et al. 2017; Ramachandran et al. 2018), and SMC (Castro et al. 2018; Ramachandran et al. 2019; Schootemeijer et al. 2021) analyses of large samples of OB stars. O stars *are* observed close to the ZAMS in young, rich star clusters

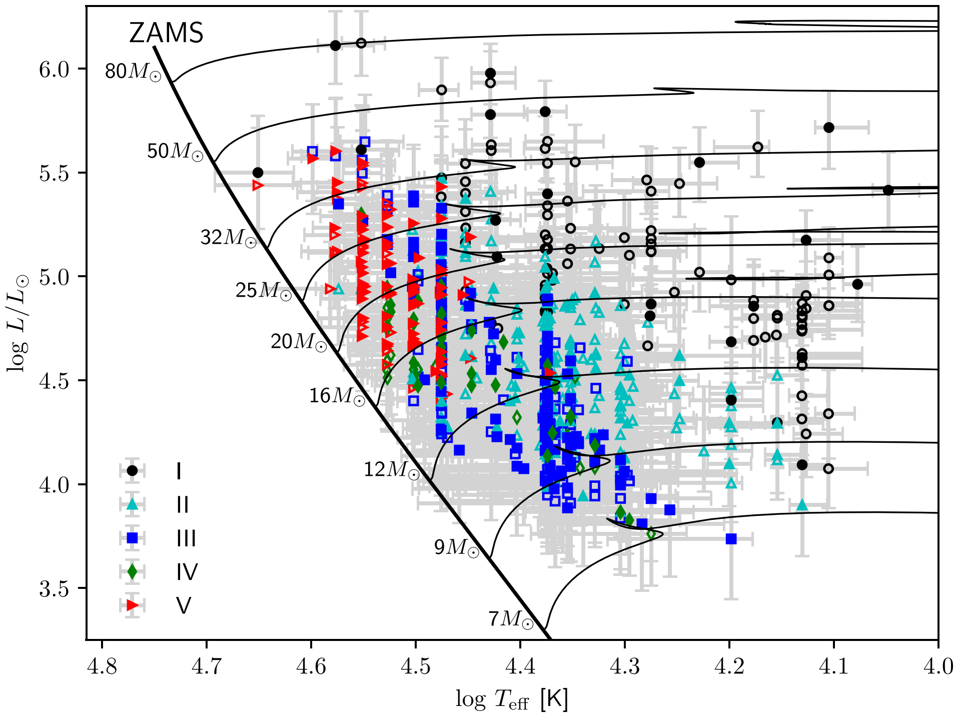

Figure 7. HR diagram of the BLOeM OB sample (colour coded by luminosity class). Open symbols are single according to analysis of the initial nine epochs of BLOeM (Bodensteiner et al. 2025; Britavskiy et al. 2025; Patrick et al. 2025; Sana et al. 2025; Villaseñor et al. 2025), filled symbols are multiple. Evolutionary tracks for SMC massive stars are from Schootemeijer et al. (2019) for non-rotating stars ($\alpha_{\rm SC} = 10$, $\alpha_{\rm OV} = 0.33$).

such as NGC 3603 in thee Milky Way (Melena et al. 2008) and R136 in the LMC (Crowther et al. 2016; Brands et al. 2022). No close counterparts to R136 exist in the SMC, with the extended star-forming region NGC 346 also deficient in luminous ZAMS stars (Rickard et al. 2022), although compact clusters whose O stars are located close to the ZAMS have been observed (Heydari-Malayeri et al. 1999a, b; Martins et al. 2004).

Aside from the deficit of ZAMS stars and those close to $T_{\rm eff} \sim$ 26 kK ($\log T_{\rm eff}$/K $\sim$ 4.4, recall Section 4.1) it is apparent that a large fraction of the BLOeM OB stars lie close to the terminal age main sequence (TAMS), although the precise TAMS is not well established from evolutionary models. One would expect very few post-MS for standard single star evolution, since evolution is predicted to be rapid toward cool supergiants. Mid to late B supergiants are unambiguously post-MS stars (see also de Burgos et al. 2025), whereas the situation for early B (super)giants is less clear (B dwarfs are too faint given the BLOeM selection criteria). From a comparison with evolutionary predictions set out in Section 7, 57 stars from the total sample of 778 are unambiguously in a post-MS evolutionary phase, providing the TAMS from Brott et al. (2011) is correct.

A major advantage of BLOeM over the majority of previous spectroscopic studies of the magellanic clouds is the multi-epoch nature of the survey. Fig. E1 provides separate HR diagrams for single (upper panel) and multiple (lower panel) systems, together with Brott et al. (2011) tracks, potentially highlighting binary interaction products (see e.g. Menon et al. 2024).

Stellar luminosities of individual BLOeM stars are provided in Table A1. The average stellar luminosity of O-type (B-type) stars in our sample is $\log(L/{\rm L}_\odot) = 5.10\pm0.31$ (4.58 ± 0.38). Tables B1 and B2 in the Appendix includes comparisons between pipeline-derived stellar luminosities of O-type (B-type) stars and those from the wider literature, for which agreement is overall satisfactory (mostly within 0.1 dex). For the 25 stars in common with Castro et al. (2018), $\log L/{\rm L}_\odot$(pipeline)$-\log L/{\rm L}_\odot$(Castro) $= +0.12\pm0.22$ dex (Appendix, Table C1). For the 30 OB stars in common with the XShootU pipeline study of Bestenlehner et al. (2025), $\log L/{\rm L}_\odot$(pipeline)$-\log L/{\rm L}_\odot$(XShootU) $= +0.11\pm0.18$.

4.3 Surface gravities

Fig. 8 shows a Kiel diagram for the analysed OB stars, with surface gravities ranging from the vicinity of $\log g \sim 4$ for O-type dwarfs, to $\log g \sim 1.5$ for late B supergiants. The average surface gravity of O-type (B-type) stars in our sample is $\log g/({\rm cm\,s^{-2}}) = 3.78\pm0.44$ (3.59 ± 0.53). Overall statistics are dominated by early B (super)giants (recall fig. 8 from Shenar et al. 2024).

Table B1 (B2) in the Appendix compares pipeline gravities of O-type (B-type) stars to literature values. Overall agreement is satisfactory. However, significantly lower gravities are inferred from the pipeline for some dwarfs and giants (e.g. BLOeM 7-072, O8 Vnn), as illustrated in Fig. 9 for OB stars. We will revisit surface gravities in Section 6.

Both H γ and H δ possess metallic lines in their damping wings, only some of which are explicitly included in FASTWIND synthetic spectra (e.g. O II $\lambda\lambda$4345-51 in Fig. 2). For the 30 OB stars in common with the XShootU pipeline study of Bestenlehner et al. (2025), $\log g$(BLOeM)$-\log g$(XShootU) $= 0.06\pm0.38$.

Spectroscopically derived surface gravities must be corrected for the effect of centrifugal forces, as highlighted by Herrero et al. (1992). Gravities corrected for centrifugal forces, denoted $g_{\rm c}$, are obtained from

$$g_{\rm c} = g + (v_{\rm e} \sin i)^2/R_*$$

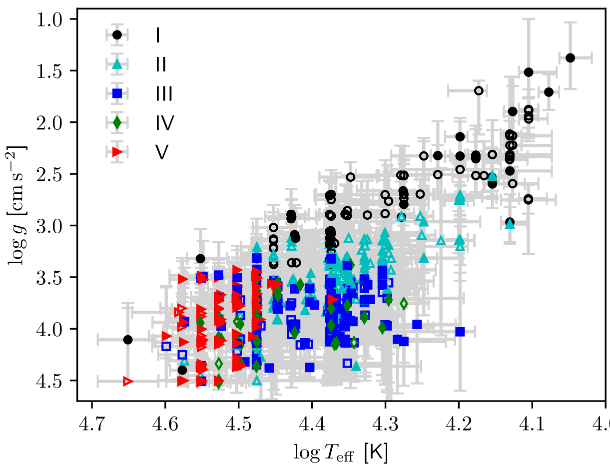

Figure 8. Comparison between effective temperatures, $T_{\rm eff}$, and surface gravities, $\log g$, of BLOeM OB stars (Kiel diagram). Open symbols are single stars according to the initial nine epochs of BLOeM (Bodensteiner et al. 2025; Britavskiy et al. 2025; Patrick et al. 2025; Sana et al. 2025; Villaseñor et al. 2025), filled symbols are multiple.

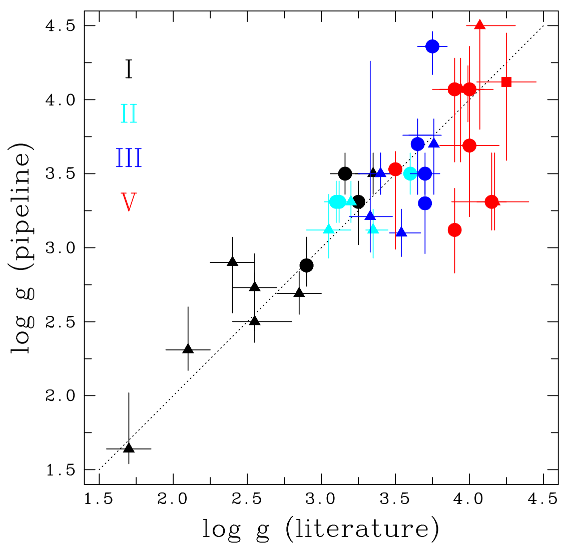

Figure 9. Comparison between $\log g$ for BLOeM OB stars from literature studies (circles: CMFGEN, triangles: FASTWIND, squares: TLUSTY) and the current pipeline, colour coded by luminosity class. References are provided in the Appendix in Tables B1 and B2.

using radii via the Stefan–Boltzmann relation, and $v_{\rm e} \sin i$ discussed in Section 5. These are included in Table A1. In most instances corrections are modest, but can exceed 0.1 dex for rapid rotators e.g. $\log g_{\rm c} - \log g = 0.40$ dex for BLOeM 6-090 (B2 III) with $v_{\rm e} \sin i \sim 400\,{\rm km\,s^{-1}}$.

4.4 Elemental abundances

Helium is our primary focus regarding elemental abundances in OB stars. The baseline He abundance from H II regions (Russell & Dopita 1990) is $N({\rm He})/N({\rm H}) = 0.09$ by number or $Y \sim 25$ per cent by mass, whereas our grid permits lower helium mass fractions to avoid a truncated PDF. Although He weak stars are known, these results should be viewed with caution. High He mass fractions for

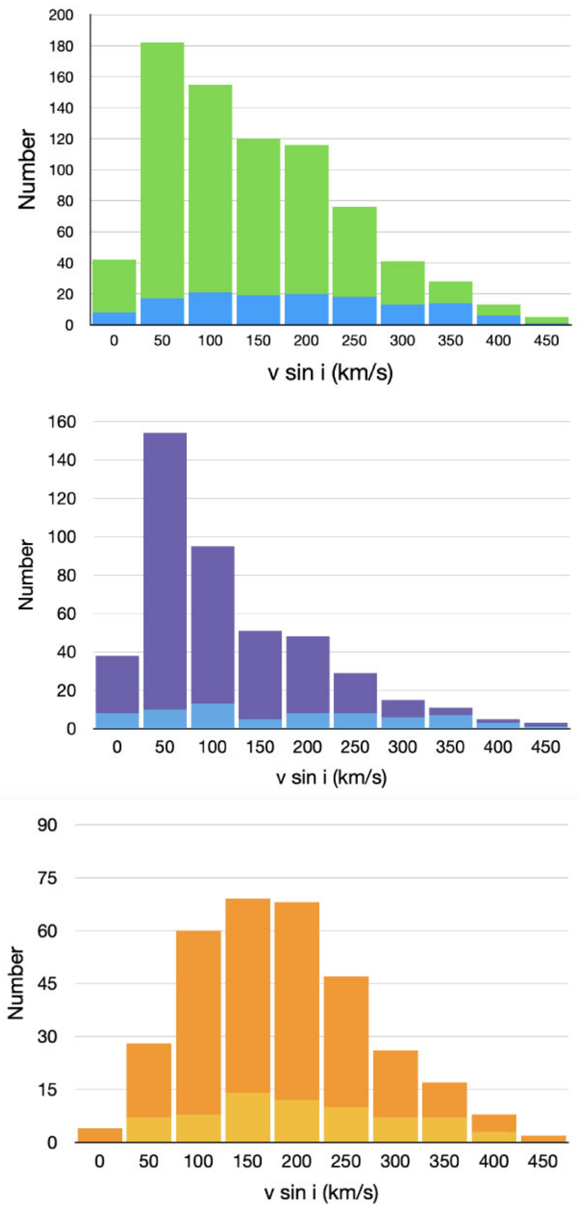

Figure 10. Histogram of projected rotational velocities $v_{\rm e} \sin i$ (${\rm km\,s^{-1}}$) of all O (blue) and B stars (green) in the top panel, sorted into $50\,{\rm km\,s^{-1}}$ bins (e.g. $50\,{\rm km\,s^{-1}}$ refers to $50\pm25\,{\rm km\,s^{-1}}$), aside from the 0 bin which refers to 0–25 ${\rm km\,s^{-1}}$; central panel: as above for single O (pale blue) and B (purple) stars according to the initial nine epochs of the BLOeM survey; lower panel: as above for multiple O (yellow) and B (orange) stars.

a significant subset of OB supergiants are more plausible, some of which infer $Y = 40$–50 per cent, with several MS stars favouring $Y = 55$ per cent, the upper limit of the grid (see also Martínez-Sebastián et al. 2025). We revisit the significance of He mass fractions for O and early B stars in Section 6.

5 ROTATIONAL VELOCITIES

5.1 Pipeline results

The distribution of projected rotational velocities for BLOeM O (blue) and B (green) stars is presented in Fig. 10 (top panel). Median values are $v_{\rm e} \sin i = 200\,{\rm km\,s^{-1}}$ ($113\,{\rm km\,s^{-1}}$) for O-type

(B-type) stars, including 8 per cent (25 per cent) of fast rotators with $v_e \sin i$ > 275 km s^{-1}. Recalling Section 3, the synthetic grid was convolved with a fixed $v_{\rm mac}$ = 20 km s^{-1}, with any additional broadening assumed to be attributed to rotation. Consequently, pipeline results will likely overestimate the true $v_e \sin i$ in many instances, and instrumental broadening hinders reliable $v_e \sin i$ for slow rotators. Table 2 provides an overview of rotational velocities obtained for our sample. Table B1 (B2) in the Appendix compares pipeline-derived rotational velocities of O-type (B-type) stars to literature results. Rotational velocities from our pipeline are similar to, or somewhat larger than, literature results.

Since close binary evolution can strongly modify rotational velocities (de Mink et al. 2014), Fig. 10 also shows histograms of rotational velocities for (apparently) single stars (middle panel) and spectroscopic binaries (lower panel), revealing strikingly different distributions. Median values for single (binary) stars are $v_e \sin i$ = 78 km s^{-1} (200 km s^{-1}). The histogram for single stars suggests a bimodality in rotational velocities for O stars, reminiscent of single early B stars from the VLT FLAMES Tarantula Survey (VFTS; Dufton et al. 2013).

This bimodality is not apparent for single B-type stars, although giants make up the overwhelming majority of BLOeM B stars (O stars are primarily dwarfs). The histogram for multiple systems reveals that high $v_e \sin i$ bins are overrepresented with respect to single stars. Nevertheless, further study is warranted since our sample includes a subset of known SB2's, which are likely to artificially boost inferred rotational velocities of binary systems. In addition, many OBe stars – usually found to be rapid rotators – are also excluded.

Fig. 11 shows the HR diagram for BLOeM OB stars, now colour coded by $v_e \sin i$, and using the non-rotating SMC metallicity tracks from Brott et al. (2011). Higher temperature OB stars (log $T_{\rm eff}$/K ≥ 4.3) exhibit a broad range of projected rotational velocities, whereas cooler B supergiants predominantly possess modest $v_e \sin i$ values. There is also a dearth of slow rotators at intermediate temperatures [log($T_{\rm eff}$/K) ∼ 4.4], suggestive of a physical origin. Fig. E2 in the Appendix separates the HR diagram into single (upper panel) and multiple (lower panel) systems, also colour coded by $v_e \sin i$, with evolutionary models from Schootemeijer et al. (2019).

Fig. 12 presents a histogram of projected rotational velocities, separated into MS (dark green) and post-MS (pale green) OB stars – according to Brott et al. (2011) rotating models discussed in Section 7 – illustrating that overall statistics are dominated by the former. The median $v_e \sin i$ of MS (post-MS) stars is 154 (55) km s^{-1}. Vink et al. (2010) have previously discussed low rotational velocities of cool B supergiants in the Milky Way and LMC.

Penny & Gies (2009) have previously estimated rotational velocities of 55 bright SMC O-type stars and B supergiants from high resolution *FUSE* spectroscopy, for which the $v_e \sin i$ distributions of both 'unevolved' (IV-V) and 'evolved' (II-I) stars peak below 100 km s^{-1}, in common with Fig. 10.

Dufton et al. (2019) have previously investigated the rotational velocities of large populations of massive stars in the NGC 346 star forming region of the SMC. They primarily focused on single B stars for which a median $v_e \sin i$ = 136 km s^{-1} was obtained, somewhat higher than our results for single B stars in the field (78 km s^{-1}). Dufton et al. (2019) compare cumulative velocity distributions of single B stars in NGC 346 with other environments in their Fig. 6, which reveals a high velocity tail. ∼10 per cent of their single B stars exceed 300 km s^{-1}, somewhat higher than the BLOeM sample of single B stars (4 per cent exceed 300 km s^{-1}).

Ramírez-Agudelo et al. (2015) have previously investigated the rotational velocities of VFTS O stars in the LMC, finding that primaries

Table 2. Summary of median masses ($M_{\rm evol}$), ages (τ), and projected rotational velocities ($v_e \sin i$) for 778 BLOeM OB stars analysed in this study, separated into single and multiple systems according to the initial nine epoch BLOeM data set (Bodensteiner et al. 2025; Britavskiy et al. 2025; Patrick et al. 2025; Sana et al. 2025; Villaseñor et al. 2025), and into main sequence (MS) versus post-MS according to rotating models from Brott et al. (2011).

Spectral type	All				Single				Multiple				Evol. phase	All			
	N	$M_{\rm evol}$ M$_\odot$	τ Myr	$v_e \sin i$ km s^{-1}	N	$M_{\rm evol}$ M$_\odot$	τ Myr	$v_e \sin i$ km s^{-1}	N	$M_{\rm evol}$ M$_\odot$	τ Myr	$v_e \sin i$ km s^{-1}		N	$M_{\rm evol}$ M$_\odot$	τ Myr	$v_e \sin i$ km s^{-1}
O	137	19.8	4.9	200	69	19.9	4.8	153	68	19.8	5.1	201	MS	721	12.8	9.6	153
B	641	12.6	10.8	113	380	12.7	10.9	78	261	12.5	10.6	156	Post-MS	57	14.2	11.3	55

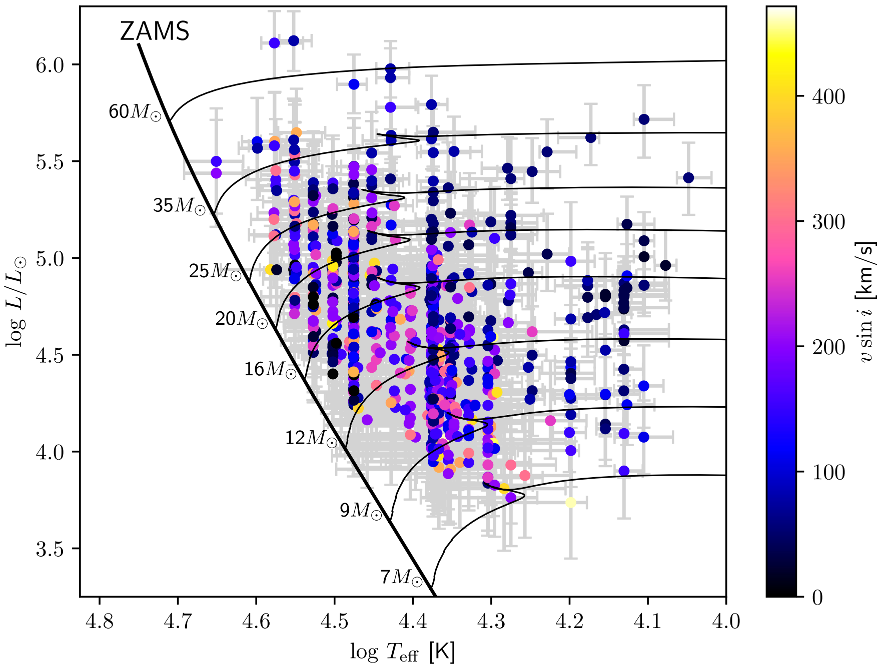

Figure 11. HR diagram of BLOeM sample (colour coded by $v_e \sin i$), together with evolutionary tracks for non-rotating SMC massive stars from Brott et al. (2011).

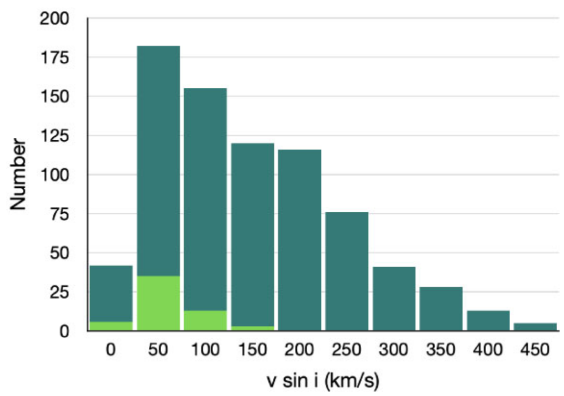

Figure 12. Histogram of projected rotational velocities $v_e \sin i$ (km s^{-1}) of MS (dark green) and post-MS (pale green) OB stars, according to Brott et al. (2011) rotating models, sorted into 50 km s^{-1} bins aside for the 0 bin (e.g. 50 km s^{-1} refers to 50±25 km s^{-1}).

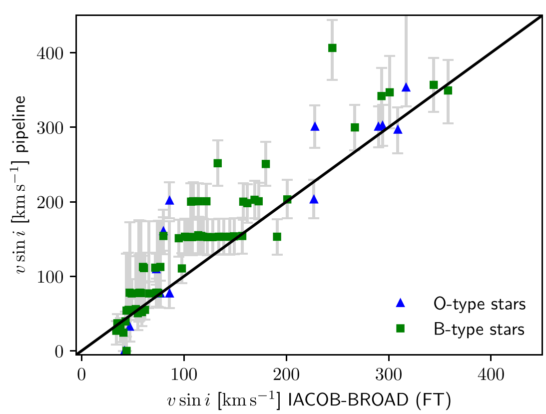

Figure 13. Comparison between $v_e \sin i$ for a subset of O (blue triangles) and B (green squares) BLOeM stars from IACOB-BROAD (Simón-Díaz & Herrero 2014) and the spectroscopic pipeline.

in binaries closely resembled those of single stars. However, wind-induced spin-down will be stronger in the LMC than the SMC, so perhaps the O star birth spin distribution is bimodal, but not retained at high metallicity due to spin-down.

5.2 Pipeline versus IACOB-BROAD results: $v_e \sin i$

To assess the reliability of pipeline-derived $v_e \sin i$, we applied the widely used tool IACOB-BROAD (Simón-Díaz & Herrero 2014) to a representative subset of the OB sample, namely BLOeM identifications with labels X-XX0. Of these, 77 stars are included in our study, recalling AF supergiants and some OB stars were excluded (SB2, OBe, strong nebulosity).

Owing to the limited spectral range of BLOeM we focus primarily on He I λ4387. Rotational velocities can be obtained either via a FT or GOF approach. In principle, the GOF method is preferred, since it also allows the determination of macroturbulence, $v_{\rm mac}$. However, this relies on suitable metal lines being available. Si III λ4553 is a suitable alternative diagnostic for the majority of the BLOeM sample, although this line is absent in O stars and late B supergiants.

We select the FT approach for comparison with pipeline results for O (blue triangles) and B (green squares) stars in Fig. 13, although results from both FT and GOF methods are provided in the Appendix in Table F1. Pipeline-derived $v_e \sin i$ typically exceed direct measurements, owing to the 'quantized' broadening values involved plus macroturbulent broadening, $v_{\rm mac}$ may be significantly higher than the 20 km s^{-1} adopted. By way of example, we have applied IACOB-BROAD to the Si III λ4553 profile in BLOeM 1-020 (B0 III), the results of which are presented in Fig. 14. Neglecting other sources of broadening, the GOF value of $v_e \sin i = 121$ km s^{-1}

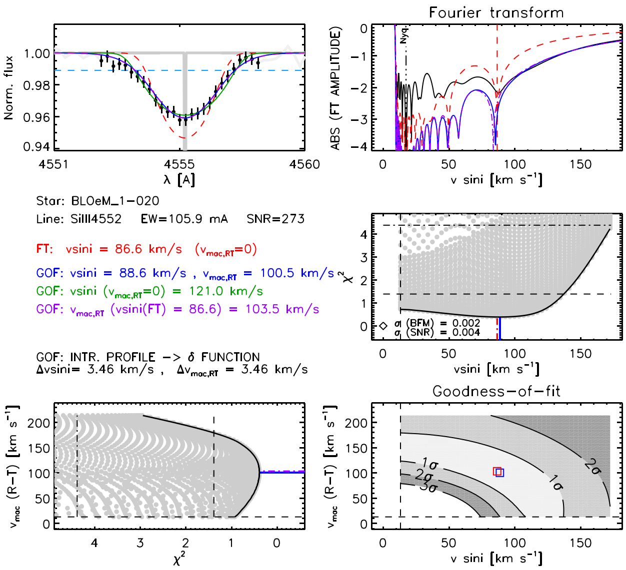

Figure 14. IACOB-BROAD (Simón-Díaz & Herrero 2014) fourier transform (FT) and goodness-of-fit (GOF) results for Si III λ4553 in BLOeM 1-020 (B0 III).

(shown in green) is in close agreement to $v_e \sin i = 113 \pm 19\,\mathrm{km\,s^{-1}}$ determined from the pipeline, with $v_e \sin i = 89\,\mathrm{km\,s^{-1}}$ obtained with a non-zero $v_{\rm mac}$ (shown in blue). In many instances – such as BLOeM 1-020 – there may be an important $v_{\rm mac}$ contribution, such that the pipeline would naturally overestimate $v_e \sin i$. In addition, potential stellar companions may also cause GOF results for strong He I lines to exceed those of weak He I and metal lines, noting that BLOeM 1-020 is a SB1 according to Villaseñor et al. (2025). Definitive results await an upcoming dedicated study of rotational velocities of BLOeM OB stars (Berlanas et al. in preparation).

6 PIPELINE VERSUS IACOB-GBAT ANALYSIS: TEMPERATURES, GRAVITIES, ABUNDANCES

Pipeline results were compared to literature temperatures, gravities, and luminosities in Section 3. Literature results were usually obtained from data sets covering a significantly broader spectroscopic range, extending to the ultraviolet in some instances (e.g. Hillier et al. 2003; Martins et al. 2024). Consequently, here we undertake a star-by-star quantitative analysis of a representative subset of the BLOeM OB stars, based on the data set outlined in Section 2.

To perform the quantitative spectroscopic analysis, we focus on the same subset as that discussed above in relation to IACOB-BROAD rotational velocities, although physical parameters could not be determined for stars lacking He II lines – classified as B1 or later. For the remainder, spectroscopic parameters ($T_{\rm eff}$, $\log g$, Y) are derived using IACOB-GBAT (Simón-Díaz et al. 2011; Sabín-Sanjulián et al. 2014; Holgado et al. 2018), together with a grid of FASTWIND models, ensuring consistent observational and stellar atmospheres to the pipeline. A velocity law with $\beta = 1$ was adopted and the wind density parameter was set to $\log Q = -13.5$. Results from the IACOB-GBAT analysis are presented in the Appendix (Table F1). Helium abundances are shown by number ratio, $y = N(\mathrm{He})/N(\mathrm{H})$, where y =0.085 corresponds to a mass fraction of $Y = 0.25$, the baseline He content in the SMC adopted by Brott et al. (2011).

Figs 15–16 present line profile fits to BLOeM 8–030 (O6.5 Vn) and 3–090 (B0.2 Ia) obtained with IACOB-GBAT. Spectral regions selected for fitting are shown in red, with regions excluded shown in blue. Overall fit quality is excellent, allowing temperatures, surface gravities and helium abundances (limits for BLOeM 3–090) to be determined in these cases.

Fig. 17 compares IACOB-GBAT results for $T_{\rm eff}$, $\log g$, and helium mass fraction Y to those from the spectroscopic pipeline. Pipeline effective temperatures are 1.5 ± 1 kK lower for O and early B stars – albeit consistent within formal uncertainties. Pipeline surface gravities for O and early B stars are also somewhat lower than IACOB-GBAT (0.1 ± 0.2 dex), albeit with considerable scatter and sizeable uncertainties.

Interactive fitting has the advantage of permitting specific regions in the wings of Balmer lines to be fit using IACOB-GBAT (e.g. excluding O II λλ4345-51 from Hγ), whereas the entire spectrum is incorporated into the spectroscopic pipeline. Finally, uniformly higher He abundances are inferred from the spectroscopic pipeline for O stars, with better consistency achieved for early B stars, albeit with considerable uncertainties in both approaches.

In summary, the comparison between results from the spectroscopic pipeline and IACOB-GBAT/IACOB-BROAD is relatively satisfactory, though caution should be advised regarding pipeline-derived surface gravities and especially He abundances.

7 STELLAR MASSES AND AGES

Individual spectroscopic masses, $M_{\rm spec}$, inferred from surface gravities and radii, are presented in Table A1. The median value of all O-type (B-type) stars is 23.0 $\mathrm{M_\odot}$ (16.4 $\mathrm{M_\odot}$). Spectroscopic masses are highly sensitive to surface gravities, which are uncertain owing to the limited spectral range of the BLOeM data set, and may also be influenced by convective turbulence (e.g. Cantiello et al. 2009). Alternatively, initial masses, $M_{\rm init}$, current masses, $M_{\rm evol}$ and ages, τ, may be determined from comparisons to evolutionary models, assuming they have evolved as single stars (which may not be the case for many of the present sample).

7.1 Evolutionary masses

For core H burning MS stars, these were obtained from a Bayesian inference method (Bronner et al., in preparation), coupled to SMC metallicity evolutionary models. This is similar to BONNSAI[3] (Schneider et al. 2014) albeit with updated techniques. Our primary evolutionary models involved the rotating grid from Brott et al. (2011), using spectroscopic temperatures, luminosities and $v_e \sin i$ as input observables. Recalling Section 4.3, we exclude spectroscopic gravities from the input observables. The only prior adopted was a Salpeter Initial Mass Function (IMF), with uniform priors for initial rotational velocities and ages. We have investigated the effect of different rotational velocity priors on the results, and obtain differences of 1–2 per cent using the empirical results from Dufton et al. (2019), a gaussian prior based on Hunter et al. (2008) or Fig. 12 rescaled by $4/\pi$.

Evolutionary masses presented are current values, $M_{\rm evol}$, with initial masses usually only a few per cent higher due to the modest mass-lost during the MS evolution at SMC metallicity. Since the upper mass limit of the SMC grid from Brott et al. (2011) was 60 $\mathrm{M_\odot}$, it was necessary to use a non-rotating SMC grid (upper limit 100 $\mathrm{M_\odot}$; Hastings et al. 2021) for two luminous O-type supergiants close to

[3]The BONNSAI web-service is available at www.astro.uni-bonn.de/stars/bonnsai

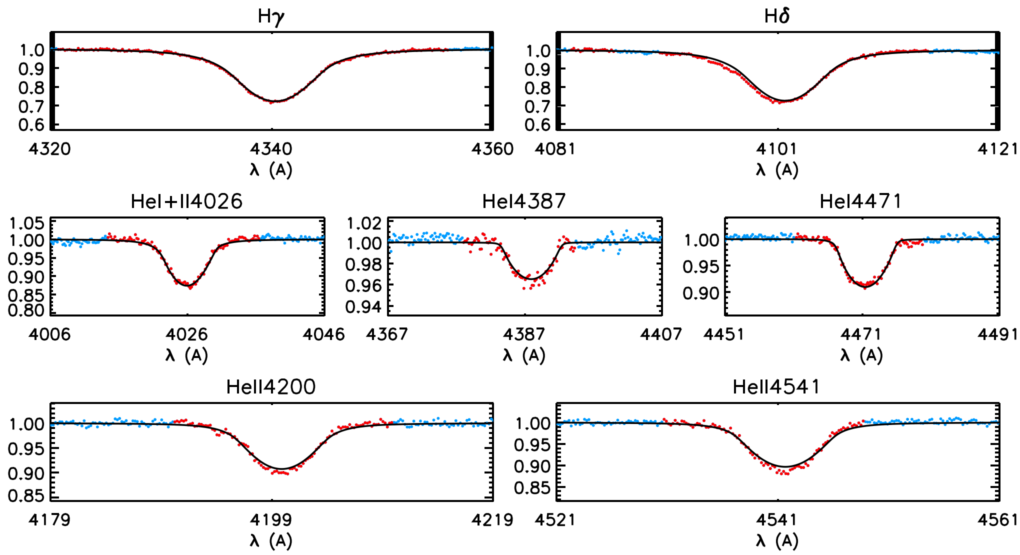

Figure 15. IACOB-GBAT hydrogen and helium spectral line fits (black lines) to BLOeM 8-030 (O6.5 Vn), in which selected regions (excluded) are indicated in red (blue). Physical parameters are $T_{\rm eff} = 38.2{\pm}0.8$ kK, $\log g = 3.82 \pm 0.08$, and $y = 0.130 \pm 0.023$, with $v_{\rm e} \sin i = 290\,{\rm km\,s^{-1}}$ (from IACOB-BROAD).

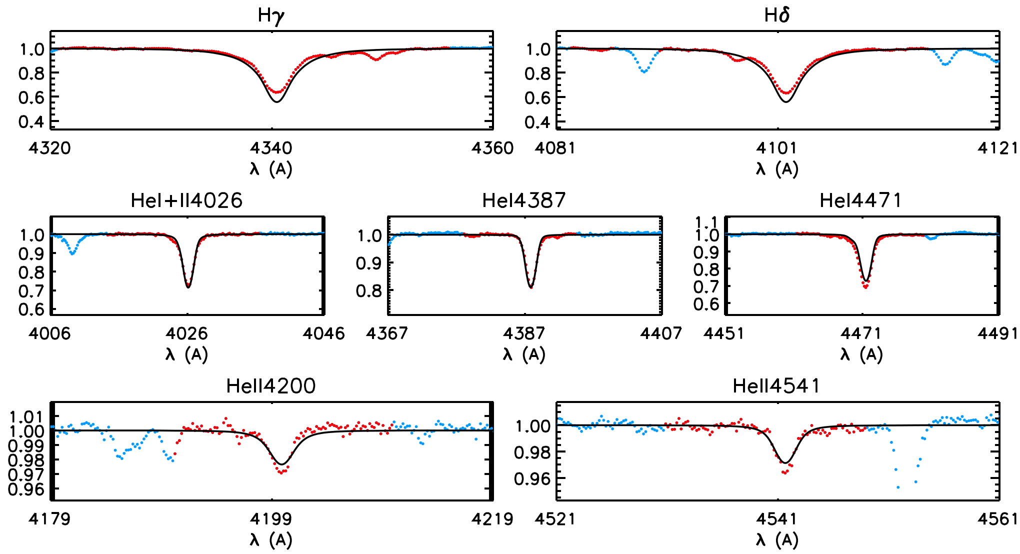

Figure 16. IACOB-GBAT hydrogen and helium spectral line fits (black lines) to BLOeM 3-090 (B0.2 Ia), in which selected regions (excluded) are indicated in red (blue). Physical parameters are $T_{\rm eff} = 28.0{\pm}1.1$ kK, $\log g = 3.19 \pm 0.21$ and $y < 0.06^{+2.3}$, with $v_{\rm e} \sin i = 74\,{\rm km\,s^{-1}}$ (from IACOB-BROAD).

this limit, namely BLOeM 3-042 (Sk 18) and BLOeM 4-058 (Sk 80), with evolutionary masses of 60^{+14}_{-12} and 61^{+15}_{-9} M$_{\odot}$, respectively.

For evolved post-MS stars, the determination of masses is more problematic since evolutionary models exhibit more variety than during the MS. However, the luminosity at the end of the contraction phase following the TAMS provides a credible mass estimate. Post-MS stars were identified as being located more than 2σ from the theoretical TAMS, again following Bronner et al. (in prep) adopting the Brott et al. (2011) rotating evolutionary models. Three sources located within 2σ from the TAMS failed the posterior predictive check (BLOeM 1-111, 2-093, 3-001) so these were also considered to be post-MS stars.

Masses obtained for post-MS stars may differ from the true value, since additional mass-loss may occur during the cool supergiant phase. Individual evolutionary masses, $M_{\rm evol}$, are included in Table A1, and assume pre-red loop evolution. SMC stars in this mass range are predicted to lose up to 5 per cent of their TAMS mass prior to core He depletion (Hastings et al. 2021). For comparison, we also obtained parameters with the grid of non-rotating models from Schootemeijer et al. (2019) using identical semiconvection ($\alpha_{\rm SC} = 10$) and overshooting ($\alpha_{\rm OV} = 0.33$) parameters to Brott et al. (2011).

We present a histogram of initial (logarithmic) masses of BLOeM OB stars in Fig. 18, separated into O (blue) and B (green) subtypes. O stars dominate the sample above 20 M$_{\odot}$ whereas B stars dominate below 16 M$_{\odot}$. The median evolutionary mass of all O-type (B-type) stars is 19.8 M$_{\odot}$ (12.6 M$_{\odot}$). Table 2 provides an overview of evolutionary masses obtained for our sample, separated into single and binary O and B stars. Subdivided into BLOeM fields (fig. 1 from Shenar et al. 2024), median OB masses range from 10.6 (Field 8) to 15.2 M$_{\odot}$ (Field 3). We shall revisit OB populations across different BLOeM fields in Section 7.3.

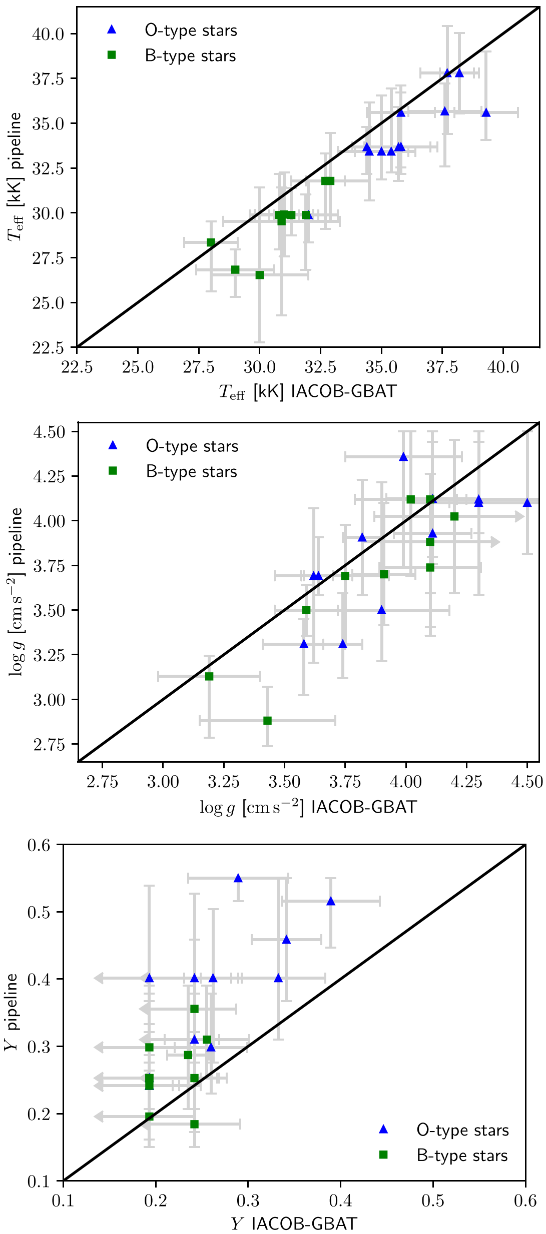

Figure 17. Comparison between IACOB-GBAT (Simón-Díaz et al. 2011) and pipeline effective temperatures for a subset of O (blue triangles) and B (green squares) BLOeM stars (top panel). Middle and lower panels: as above for $\log g$ and helium mass fraction, Y, respectively. $Y = 0.25$ is the SMC baseline according to Brott et al. (2011).

The target selection criteria for the BLOeM survey focused on stars with initial masses in excess of 8 $M_\odot$ (Shenar et al. 2024). Indeed, Fig. 18 reveals a sharp cut-off to masses at $\log M_{\rm init}/M_\odot = 0.9$ or 8 $M_\odot$. A key goal of BLOeM is to determine the slope of the IMF of massive stars in the SMC. We defer a determination of the IMF to a future study in this series once all epochs have been collected (late 2025). The complete multi-epoch data set will permit a more robust census of single stars to be established, together with a careful analysis of binaries from which individual component masses will be determined.

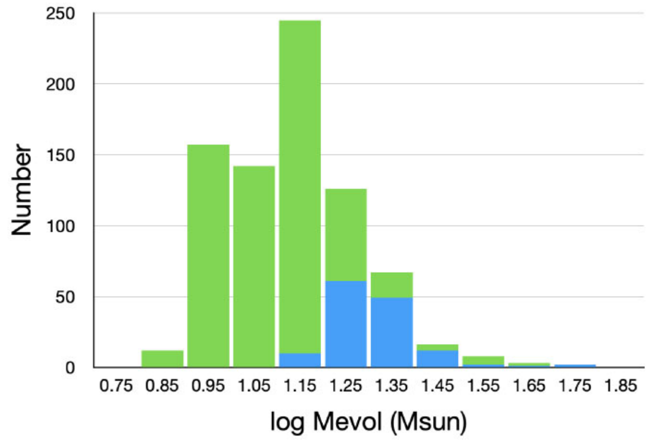

Figure 18. Histogram of (logarithmic) current masses ($M_\odot$) of BLOeM O (blue) and B (green) stars, with O stars dominant for $\log M_{\rm evol}/M_\odot \geq 1.35 \pm 0.05$ and B stars dominant for $\log M_{\rm evol}/M_\odot \leq 1.15 \pm 0.05$. Masses are based on Brott et al. (2011) rotating evolutionary models, plus Hastings et al. (2021) evolutionary models for two luminous O supergiants.

7.2 Spectroscopic versus evolutionary masses

Fig. 19 compares spectroscopic and (current) evolutionary masses of OB stars from the BLOeM survey (filled symbols are known binaries) based on Brott et al. (2011) rotating models. Overall, $M_{\rm spec} \geq M_{\rm evol}$, with the possible exception of supergiants (black symbols). Comparisons are hindered by large uncertainties in $\log g_{\rm c}$, plus some of the stars are likely products of binary interaction for which evolutionary masses will be in error. In contrast, the original mass discrepancy between spectroscopic and evolutionary values for OB stars identified by Herrero et al. (1992) involved $M_{\rm evol} \geq M_{\rm spec}$.

Schneider et al. (2018) failed to identify a statistically significant mass discrepancy amongst OB stars from the VFTS survey of 30 Doradus in the LMC (Evans et al. 2011) and no major discrepancy was identified by Bestenlehner et al. (2025) for pipeline results of higher luminosity LMC and SMC OB stars from the XShootU survey. For completeness, Fig. G1 compares spectroscopic masses to evolutionary masses obtained with non-rotating SMC models from Schootemeijer et al. (2019), which also reveals $M_{\rm spec} \geq M_{\rm evol}$.

For the BLOeM sample, the discrepancy may arise as a result of the limited spectral window available (recall Fig. 17) or the focus on non-supergiant B stars. Indeed, Schneider et al. (2018) found $M_{\rm spec} \geq M_{\rm evol}$ for B dwarfs within the VFTS sample. Regardless, various explanations for the discrepancy have been proposed. Recall that spectroscopic gravities are sensitive to turbulent velocities, for which a fixed value of 20 km s^{-1} is adopted in our study. 2D simulations suggest significantly higher turbulent broadening (Debnath et al. 2024), albeit dependent on metallicity (Cantiello et al. 2009).

7.3 Stellar ages

Stellar ages following the same approach as that described above for evolutionary masses and are included in Table A1. Since Brott et al. (2011) evolutionary models were adopted, inferred MS lifetimes are believed to be underestimated by ∼15 per cent (Marchant 2017; see fig 5.2) with respect to MESA models (Paxton et al. 2011, 2015). Fig. 20 presents a histogram of ages of O (green) and B (blue) subtypes, with median stellar ages of 4.9 and 10.8 Myr, respectively, reflecting the shorter lifetimes of higher mass stars. The youngest O

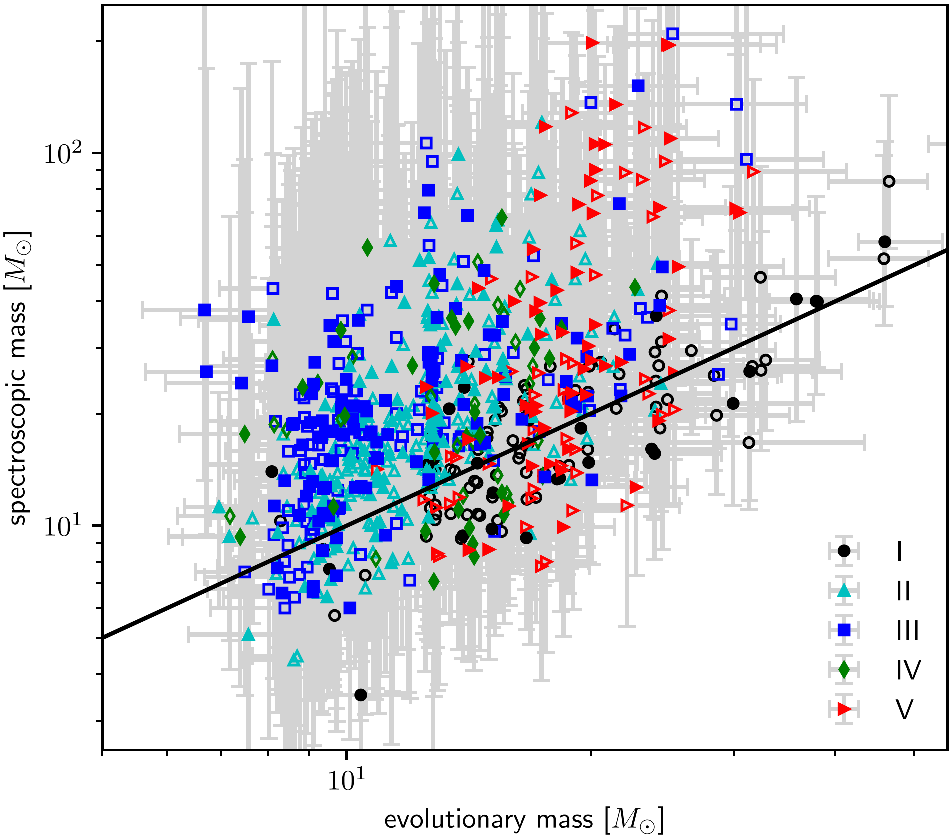

Figure 19. Comparison between (current) evolutionary masses and spectroscopic masses of BLOeM OB stars, based on Brott et al. (2011) rotating models, plus Hastings et al. (2021) evolutionary models for two luminous O supergiants above the upper mass limit of the Brott et al. (2011) models (BLOeM 3-042 and 4-058), colour coded by luminosity class (filled symbols are binaries).

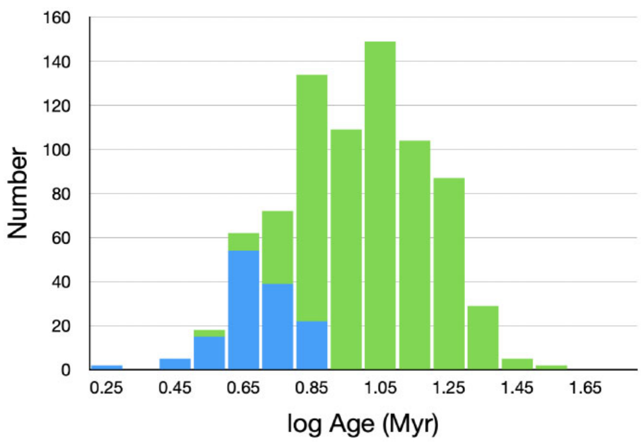

Figure 20. Histogram of (logarithmic) ages (in Myr) of BLOeM O (blue) and B (green) stars, based on Brott et al. (2011) rotating evolutionary models, plus Hastings et al. (2021) evolutionary models for two luminous O supergiants.

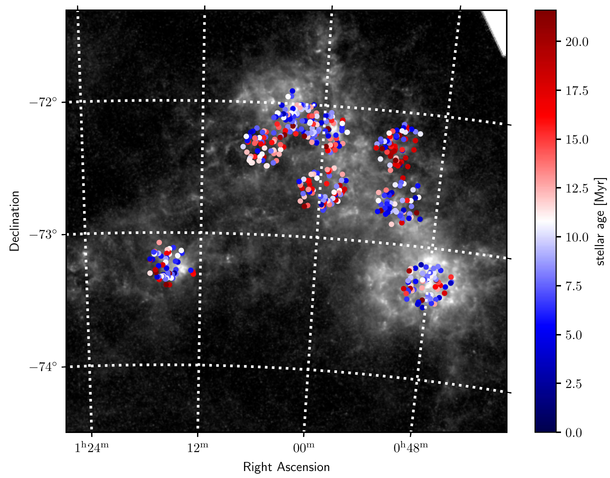

Figure 21. Ages of BLOeM OB stars, overlaid on a *Herschel* SPIRE 350 μm map of the SMC (Meixner et al. 2013). Field 8 (upper right) hosts OB stars with the highest median age (13.1 Myr) with the remainder in the range 7.7–11 Myr.

stars have ages of ∼3 Myr (e.g. BLOeM 4-058) whereas the oldest B stars reach 30 Myr (e.g. BLOeM 6-062).

Fig. 21 overlays ages of OB stars on a *Herschel* SPIRE 350 μm dust map of the SMC (Meixner et al. 2013). Subdivided into BLOeM fields (fig. 1 from Shenar et al. 2024), median OB ages range from 7.7 (Field 1) to 13.1 Myr (Field 8). Table 2 provides an overview of evolutionary ages obtained for our sample.

Of course, a large fraction of BLOeM OB targets comprise binary systems, so inferred masses (ages) represent upper (lower) limits to the primary component. In addition, mass exchange during close binary evolution can rejuvenate mass gainers, giving the false appearance of youth, so detailed masses and ages await analysis of the complete time series BLOeM data set.

8 BLOEM IN THE CONTEXT OF THE GLOBAL SMC O STAR POPULATION

BLOeM was designed to sample representative O and early B stars in the SMC, with 929 science targets drawn from a master *Gaia* catalogue of 5576 stars representing 1/6 of the global population (Shenar et al. 2024). Bonanos et al. (2010) have previously provided a catalogue of 5324 massive stars in the SMC comprising literature spectral types. This included 277 O-type stars, plus the 12 known Wolf–Rayet-type stars in the SMC (5 of which also host O stars).

At face value this suggests that the BLOeM survey – including 159 O stars – comprises over half of the known O stars within the SMC. However, nearly 50 per cent of the O stars from BLOeM were newly classified as such, either representing the first spectral classification or a revision from the previous literature. We have therefore compiled an updated catalogue of spectroscopically confirmed O stars in the SMC, adapted from I.D. Howarth (private communication), to incorporate newly identified O stars from BLOeM plus additions from e.g. 2dFS (Evans et al. 2004a), RIOTS4 (Lamb et al. 2016) and Dufton et al. (2019). This is presented in RA order in Table H1 (see supplementary data).

O type classifications solely based from UV spectroscopy are excluded (e.g. Prinja 1987; Smith Neubig & Bruhweiler 1997) from the present compilation. However, we do include the embedded ionizing source of the compact H II region N88A (Heydari-Malayeri et al. 1999b; Testor et al. 2010), owing to its high ionizing photon production rate, although this itself may comprise multiple O star components. A number of stars have been classified as either O9.5 or B0, so the updated catalogue of SMC O stars provided in Table H1 includes alternate classifications. 75 BLOeM sources are newly identified as O stars which brings the current total of systems to 449, so BLOeM comprises 1/3 of the known O star population of the SMC, of which ∼10 per cent lie within the NGC 346 star-forming region. The current total will doubtless be incomplete, with the upcoming VISTA/4MOST spectroscopic survey 1001MC (Cioni et al. 2019) set to provide definitive numbers.

There is a well known deficiency of luminous early O stars in the SMC (Schootemeijer et al. 2021), so it is unsurprising that the earliest O-type stars within the sample are BLOeM 2-079 (O4: V + early B) and BLOeM 3-049 (O4 I(n)). At present, there are six known O2–3 stars in the SMC, NGC 346 MPG 355 (Walborn et al. 2004), NGC 346 MPG 435 (Dufton et al. 2019; Rickard & Pauli 2023), NGC 346 ELS 7 (Bestenlehner et al. 2025), Sk 183 (Evans et al. 2012; Ramachandran et al. 2019), AzV 14 (Pauli et al. 2023), and AzV 435 (Massey et al. 2005), plus several O3.5 stars (Bestenlehner et al. 2025).

Individual BLOeM stars for which $\log(Q_0/\mathrm{s}^{-1}) \geq 49.0$ are listed in Table 3, which also includes their ionizing output in the neutral He continuum, Q_1, and the ratio of these rates. Collectively these 17 sources provide $Q_0 = 3.2 \times 10^{50}\,\mathrm{s}^{-1}$, over 40 per cent of the cumulative $Q_0 = 7.5 \times 10^{50}\,\mathrm{s}^{-1}$ Lyman continuum ionizing output of the 778 BLOeM OB stars. For context, this represents ∼20 per cent of the global Hα-derived $Q_0 = 3.4 \times 10^{51}\,\mathrm{s}^{-1}$ ionizing output of the SMC (Kennicutt et al. 2008). Since BLOeM samples 1/3 of the known SMC O population one might have anticipated a greater fraction. However, the earliest O stars and Wolf–Rayet stars – neither populations included in BLOeM – are anticipated to dominate the ionizing output of individual H II regions or more generally the galaxy as a whole (Doran et al. 2013; Ramachandran et al. 2019).

Table 3. Lyman continuum ionizing photon rates of BLOeM OB stars exceeding $Q_0 = 10^{49}\,\mathrm{s}^{-1}$, including neutral He continuum ionizing photon rates (Q_1), and their ratio $\log Q_1/Q_0$.

BLOeM	Sk	AzV	Spectral type	$\log Q_0$ s^{-1}	$\log Q_1$ s^{-1}	$\log Q_1/Q_0$
4-058	80	232	O7 Iaf$^+$	49.73	48.75	–0.98
3-042	18	26	O6 I(f) + O7.5	49.70	48.83	–0.87
1-072	–	–	O5 V(n) + O6.5(n)	49.33	48.49	–0.84
2-016	–	80	O6 III:nn(f)p	49.33	48.42	–0.90
2-020	–	83	O7 Iaf$^+$	49.28	48.36	–0.92
3-081	–	–	O6 III:	49.28	48.52	–0.75
3-049	–	–	O4 I(n)	49.27	48.66	–0.61
7-069	84	243	O6.5 V	49.22	48.47	–0.75
6-033	–	–	O4.5 V:	49.19	48.60	–0.59
1-102	–	345a	O6 III(n)	49.17	48.30	–0.87
2-035	–	95	O7.5 III((f))	49.10	48.13	–0.97
2-075	–	133	O6 Vn((f))	49.08	48.14	–0.94
6-105	–	–	O6 V:n	49.08	48.20	–0.88
3-051	–	–	O5.5: V	49.07	48.31	–0.75
2-098	–	–	O6.5 V((f))	49.00	48.15	–0.86
2-007	35	70	O9.5 II-I	49.00	46.53	–2.47

9 CONCLUSIONS

Previous quantitative studies have included large samples of OB stars in the Milky Way (Castro et al. 2014; de Burgos et al. 2024; Holgado et al. 2020, 2022) and magellanic clouds (Ramírez-Agudelo et al. 2017; Sabín-Sanjulián et al. 2017; Castro et al. 2018; Ramachandran et al. 2019; Bestenlehner et al. 2025). Nevertheless, the present study – involving a large and representative sample of hot, massive stars in the SMC – is unprecedented in its scale, owing to the use of a dedicated spectroscopic pipeline (Bestenlehner et al. 2024) applied to large grids of synthetic spectra computed with FASTWIND (Puls et al. 2005; Rivero González et al. 2012).

We limit our analysis to those OB stars unaffected by strong disc emission, so OBe, sgB[e] stars are excluded, together with instances of strong nebular emission and/or significant contamination from secondaries in SB2 systems. Our study therefore focuses on a total of 778 stars, or 92 per cent of the total OB sample from BLOeM.

Stellar temperatures are generally in line with previous determinations for SMC OB stars, except that the pipeline fails to reproduce Si IV λ4089 in some instances, so underestimates the temperatures of some early B stars. Nevertheless, stellar temperatures (Fig. 6) and surface gravities (Fig. 9) are generally in satisfactory agreement with previous detailed studies based on extensive UV and optical spectroscopy.

Temperatures are also in good agreement with pipeline analysis of BLOeM stars in common with XShootU (Bestenlehner et al. 2025) plus IACOB-GBAT bespoke results for a subset of BLOeM O and early B stars (Fig. 17). There is greater scatter for surface gravity comparisons, and He abundance comparisons with IACOB-GBAT suggesting the pipeline overestimates He abundances. Both may arise from the limited spectral range of the current BLOeM data set.

We establish median BLOeM O (B) masses of 19.8 (12.6) $\mathrm{M}_\odot$ with a few O supergiants exceeding 50 $\mathrm{M}_\odot$ (e.g. BLOeM 4-058 a.k.a. Sk 80), and a significant fraction close to the theoretical TAMS according to rotating models of Brott et al. (2011). Evolution is expected to be rapid between the TAMS and cool supergiant phase for single stars, so the presence of such stars is difficult to explain without considering binary evolution unless the theoretical TAMS extend to cooler temperatures. A comparison between spectroscopic and evolutionary masses (Fig. 19) reveals systematically higher values for the former, with the potential exception of OB supergiants.

The pipeline analysis also provides estimates of rotational velocities, $v_e \sin i$, with known binaries (mostly SB1) possessing relatively high rotational velocities, and an apparent bimodality amongst single O stars (Fig. 10) which resembles that of single B stars in the Tarantula region of the LMC identified by Dufton et al. (2013). Definitive results await an upcoming dedicated study (Berlanas et al. in preparation), although pipeline results are broadly in line with IACOB-BROAD FT results from He I λ4387 for a subset of BLOeM OB stars (Fig. 13).

Future studies will utilize the entire 25 epoch BLOeM data set, permitting the identification of additional binaries, derive orbital properties for known SB1 and SB2 systems, individual fits for disentangled spectra, allowing searches for compact companions, and determine the IMF of single stars and binaries.

ACKNOWLEDGEMENTS

Based on observations collected at the European Southern Observatory under programme id 112.25W2. JMB and PAC acknowledge financial support from the Science and Technology Facilities Council via research grant ST/V000853/1 (P.I. Vik Dhillon). This work had received funding from the European Research Council (ERC) under the European Union's Horizon 2020 research and innovation programme (grant agreements 945806/TEL-STARS, 101164755/METAL, 101165213/Star-Grasp). VAB and FRNS acknowledge support from the Klaus Tschira Foundation and the Deutsche Forschungsgemeinschaft (DFG, German Research Foundation) under Germany's Excellence Strategy EXC 2181/1-390900948 (the Heidelberg STRUCTURES Excellence Cluster). SS-D acknowledges support from the Spanish Ministry of Science and Innovation and Universities (MICIU) through the Spanish State Research Agency (AEI) through grants PID2021-122397NB-C21 and the Severo Ochoa Programme 2020–2023 (CEX2019-000920-S). PM acknowledges support from the FWO senior fellowship number 12ZY523N. TS is supported by the Israel Science Foundation (ISF) under grant number 2434/24. This research has made extensive use of the SIMBAD data base, operated at CDS, Strasbourg, France, the FASTWIND stellar atmosphere code developed by Joachim Puls, the National Institute of Standards and Technology (NIST) atomic spectra data base, the Vienna Atomic Line Data base (VALD), and SCIPY https://scipy.org/citing-scipy/. We appreciate comments on the draft manuscript by Abel Schootemeijer and Jorick Vink.

Based on observations collected at the European Southern Observatory under ESO programme ID 112.25W2.

DATA AVAILABILITY

Tables A1 (physical properties of BLOeM OB stars) and H1 (catalogue of spectroscopically confirmed O stars in the SMC) are available in electronic form at the CDS via anonymous ftp to cdsarc.u-strasbg.fr (130.79.128.5) or via http://cdsweb.u-strasbg.fr/cgi-bin/qcat?J/A + A/.

Online material at 10.5281/zenodo.15526149 includes spectral fits for each star (model in red, observations in blue).

REFERENCES

Abbott B. P. et al., 2016, Phys. Rev. X, 6, 041015
Becker S. R., Butler K., 1988, A&A, 201, 232
Becker S. R., Butler K., 1990, A&A, 235, 326
Bestenlehner J. M., Enßlin T., Bergemann M., Crowther P. A., Greiner M., Selig M., 2024, MNRAS, 528, 6735
Bestenlehner J. M., Crowther P. A., Hawcroft C., Sana H., Tramper F., Vink J. S., Brands S. A., Sander A. A. C., 2025, A&A, 695, A198
Bodensteiner J. et al., 2025, A&A, 698, A38
Bonanos A. Z. et al., 2010, AJ, 140, 416
Bouret J. C., Lanz T., Martins F., Marcolino W. L. F., Hillier D. J., Depagne E., Hubeny I., 2013, A&A, 555, A1 (BLM13)
Bouret J. C., Martins F., Hillier D. J., Marcolino W. L. F., Rocha-Pinto H. J., Georgy C., Lanz T., Hubeny I., 2021, A&A, 647, A134 (BMH21)
Brands S. A. et al., 2022, A&A, 663, A36
Britavskiy N. et al., 2025, A&A, 698, A40
Brott I. et al., 2011, A&A, 530, A115
Cantiello M. et al., 2009, A&A, 499, 279
Castro N., Fossati L., Langer N., Simón-Díaz S., Schneider F. R. N., Izzard R. G., 2014, A&A, 570, L13
Castro N., Oey M. S., Fossati L., Langer N., 2018, ApJ, 868, 57
Cioni M. R. L. et al., 2011, A&A, 527, A116
Cioni M. R. L. et al., 2019, The Messenger, 175, 54
Crowther P. A. et al., 2016, MNRAS, 458, 624
de Burgos A., Simón-Díaz S., Urbaneja M. A., Puls J., 2024, A&A, 687, A228
de Burgos A., Simón-Díaz S., Urbaneja M. A., Holgado G., Ekström S., Ramírez-Tannus M. C., Zari E., 2025, A&A, 695, A87
de Mink S. E., Sana H., Langer N., Izzard R. G., Schneider F. R. N., 2014, ApJ, 782, 7
Debnath D., Sundqvist J. O., Moens N., Van der Sijpt C., Verhamme O., Poniatowski L. G., 2024, A&A, 684, A177
Doran E. I. et al., 2013, A&A, 558, A134
Dufton P. L. et al., 2013, A&A, 550, A109
Dufton P. L. et al., 2018, A&A, 615, A101
Dufton P. L., Evans C. J., Hunter I., Lennon D. J., Schneider F. R. N., 2019, A&A, 626, A50
Evans C. J., Howarth I. D., 2008, MNRAS, 386, 826
Evans C. J., Howarth I. D., Irwin M. J., Burnley A. W., Harries T. J., 2004a, MNRAS, 353, 601
Evans C. J., Crowther P. A., Fullerton A. W., Hillier D. J., 2004b, ApJ, 610, 1021 (ECF04)
Evans C. J., Lennon D. J., Smartt S. J., Trundle C., 2006, A&A, 456, 623
Evans C. J. et al., 2011, A&A, 530, A108
Evans C. J. et al., 2012, ApJ, 753, 173
Gaia Collaboration, 2021, A&A, 649, A1
Geen S. et al., 2023, PASP, 135, 021001
Gehrels N., Ramirez-Ruiz E., Fox D. B., 2009, ARA&A, 47, 567
Gordon K. D. et al., 2024, ApJ, 970, 51
Graczyk D. et al., 2020, ApJ, 904, 13
Hardorp J., Scholz M., 1970, ApJS, 19, 193
Hastings B., Langer N., Wang C., Schootemeijer A., Milone A. P., 2021, A&A, 653, A144
Herrero A., Kudritzki R. P., Vilchez J. M., Kunze D., Butler K., Haser S., 1992, A&A, 261, 209
Heydari-Malayeri M., Rosa M. R., Zinnecker H., Deharveng L., Charmandaris V., 1999a, A&A, 344, 848
Heydari-Malayeri M., Charmandaris V., Deharveng L., Rosa M. R., Zinnecker H., 1999b, A&A, 347, 841
Hilditch R. W., Howarth I. D., Harries T. J., 2005, MNRAS, 357, 304
Hillier D. J., Miller D. L., 1998, ApJ, 496, 407
Hillier D. J., Lanz T., Heap S. R., Hubeny I., Smith L. J., Evans C. J., Lennon D. J., Bouret J. C., 2003, ApJ, 588, 1039 (HLH03)
Holgado G. et al., 2018, A&A, 613, A65
Holgado G. et al., 2020, A&A, 638, A157
Holgado G., Simón-Díaz S., Herrero A., Barbá R. H., 2022, A&A, 665, A150
Hubeny I., Lanz T., 1995, ApJ, 439, 875
Hunter I. et al., 2007, A&A, 466, 277 (HDS07)
Hunter I. et al., 2008, A&A, 479, 541
Kennicutt R. C., Jr., Lee J. C., Funes J. G. J. S., Sakai S., Akiyama S., 2008, ApJS, 178, 247
Kilian J., Montenbruck O., Nissen P. E., 1991, A&AS, 88, 101

Lamb J. B., Oey M. S., Segura-Cox D. M., Graus A. S., Kiminki D. C., Golden-Marx J. B., Parker J. W., 2016, ApJ, 817, 113
Mahy L. et al., 2020, A&A, 634, A118
Maíz Apellániz J. et al., 2014, A&A, 564, A63
Marchant P., 2017, PhD thesis, Univ. Bonn, Germany
Martínez-Sebastián C., Simón-Díaz S., Jin H., Keszthelyi Z., Holgado G., Langer N., Puls J., 2025, A&A, 693, L10
Martins F., Schaerer D., Hillier D. J., Heydari-Malayeri M., 2004, A&A, 420, 1087
Martins F. et al., 2024, A&A, 689, A31 (MBH24)
Massey P., 2002, ApJS, 141, 81
Massey P., Parker J. W., Garmany C. D., 1989, AJ, 98, 1305
Massey P., Bresolin F., Kudritzki R. P., Puls J., Pauldrach A. W. A., 2004, ApJ, 608, 1001 (MBK04)
Massey P., Puls J., Pauldrach A. W. A., Bresolin F., Kudritzki R. P., Simon T., 2005, ApJ, 627, 477
Massey P., Zangari A. M., Morrell N. I., Puls J., DeGioia-Eastwood K., Bresolin F., Kudritzki R.-P., 2009, ApJ, 692, 618 (MZM09)
Meixner M. et al., 2013, AJ, 146, 62
Melena N. W., Massey P., Morrell N. I., Zangari A. M., 2008, AJ, 135, 878
Menon A. et al., 2024, ApJ, 963, L42
Mokiem M. R. et al., 2006, A&A, 456, 1131 (MKE06)
Pasquini L. et al., 2002, The Messenger, 110, 1
Patrick L. R. et al., 2025, A&A, 698, A39
Pauli D. et al., 2023, A&A, 673, A40
Paxton B., Bildsten L., Dotter A., Herwig F., Lesaffre P., Timmes F., 2011, ApJS, 192, 3
Paxton B. et al., 2015, ApJS, 220, 15
Penny L. R., Gies D. R., 2009, ApJ, 700, 844
Prinja R. K., 1987, MNRAS, 228, 173
Puls J., Urbaneja M. A., Venero R., Repolust T., Springmann U., Jokuthy A., Mokiem M. R., 2005, A&A, 435, 669
Ramachandran V., Hamann W. R., Hainich R., Oskinova L. M., Shenar T., Sander A. A. C., Todt H., Gallagher J. S., 2018, A&A, 615, A40
Ramachandran V. et al., 2019, A&A, 625, A104
Ramírez-Agudelo O. H. et al., 2015, A&A, 580, A92
Ramírez-Agudelo O. H. et al., 2017, A&A, 600, A81
Rickard M. J., Pauli D., 2023, A&A, 674, A56
Rickard M. J. et al., 2022, A&A, 666, A189
Rivero González J. G., Puls J., Najarro F., Brott I., 2012, A&A, 537, A79
Roman-Duval J. et al., 2025, ApJ, 985, 109
Russell S. C., Dopita M. A., 1990, ApJS, 74, 93
Sabín-Sanjulián C. et al., 2014, A&A, 564, A39
Sabín-Sanjulián C. et al., 2017, A&A, 601, A79
Sana H. et al., 2012, Science, 337, 444
Sana H. et al., 2013, A&A, 550, A107
Sana H. et al., 2025, Nat. Astron., accepted
Schneider F. R. N., Langer N., de Koter A., Brott I., Izzard R. G., Lau H. H. B., 2014, A&A, 570, A66
Schneider F. R. N. et al., 2018, A&A, 618, A73
Schootemeijer A., Langer N., Grin N. J., Wang C., 2019, A&A, 625, A132
Schootemeijer A. et al., 2021, A&A, 646, A106
Shenar T. et al., 2022, A&A, 665, A148
Shenar T. et al., 2024, A&A, 690, A289
Simón-Díaz S., Herrero A., 2014, A&A, 562, A135
Simón-Díaz S., Castro N., Herrero A., Puls J., Garcia M., Sabín-Sanjulián C., 2011, J. Phys. Conf. Ser., 328, 012021
Simón-Díaz S., Godart M., Castro N., Herrero A., Aerts C., Puls J., Telting J., Grassitelli L., 2017, A&A, 597, A22
Skrutskie M. F. et al., 2006, AJ, 131, 1163
Smartt S. J., 2015, Publ. Astron. Soc. Aust., 32, e016
Smith Neubig M. M., Bruhweiler F. C., 1997, AJ, 114, 1951
Testor G., Lemaire J. L., Heydari-Malayeri M., Kristensen L. E., Diana S., Field D., 2010, A&A, 510, A95
Trundle C., Lennon D. J., 2005, A&A, 434, 677 (TL05)
Trundle C., Lennon D. J., Puls J., Dufton P. L., 2004, A&A, 417, 217 (TLP04)
Villaseñor J. I. et al., 2025, A&A, 698, A41
Vink J. S., Brott I., Gräfener G., Langer N., de Koter A., Lennon D. J., 2010, A&A, 512, L7
Vink J. S. et al., 2023, A&A, 675, A154
Walborn N. R., 1983, ApJ, 265, 716
Walborn N. R., Morrell N. I., Howarth I. D., Crowther P. A., Lennon D. J., Massey P., Arias J. I., 2004, ApJ, 608, 1028
Wang B., Shi W., Miao Z., 2015, PLoS ONE, 10, e0118537
Wenåker I., 1990, Phys. Scr, 42, 667

SUPPORTING INFORMATION

Supplementary data are available at *MNRAS* online.

BLOeM-pipeline_MNRAS_final_A1_H1_v2.pdf

Please note: Oxford University Press is not responsible for the content or functionality of any supporting materials supplied by the authors. Any queries (other than missing material) should be directed to the corresponding author for the article.

APPENDIX A: PHYSICAL PROPERTIES OF BLOEM OB STARS

Table A1 is available in supplementary data and in electronic form at http://cdsweb.u-strasbg.fr/cgi-bin/qcat?J/A+A/.

APPENDIX B: PIPELINE VERSUS LITERATURE RESULTS

Tables B1 and B2 compare pipeline-derived physical parameters of BLOeM O and B stars, respectively, with representative literature results.

Table B1. Comparison of pipeline-derived physical parameters of BLOeM O stars with representative literature results. Previous analyses involve FASTWIND (Puls et al. 2005; Rivero González et al. 2012) or CMFGEN (Hillier & Miller 1998).

BLOeM	Alias	Spect. type	$T_{\rm eff}$ kK	$\log g$ cm s^{-2}	$\log L$ L$_\odot$	$v_{\rm e} \sin i$ km s^{-1}	Fitting tool	Ref.
2-016	AzV 80	O6 III:nn(f)p	38.0	3.70	5.71	350	CMFGEN (He)	MBH24
			$35.4^{+1.9}_{-3.1}$	$3.30^{+0.17}_{-0.34}$	$5.65^{+0.23}_{-0.24}$	357^{+131}_{-30}	Pipeline	This work
7-069	AzV 243	O6.5 V	$42.6^{+0.8}_{-0.6}$	$3.94^{+0.09}_{-0.07}$	5.68±0.07	59^{+8}_{-6}	FASTWIND (He)	MKE06
			39.6±1.5	3.90±0.10	5.59±0.10	60	CMFGEN (He)	BLM13
			$39.7^{+2.2}_{-3.4}$	$4.07^{+0.22}_{-0.49}$	$5.57^{+0.26}_{-0.27}$	154^{+25}_{-25}	Pipeline	This work
4-057	NGC346 ELS 46	O6.5 Vnn	$39.7^{+1.7}_{-1.8}$	$4.17^{+0.23}_{-0.29}$	4.81±0.10	340^{+45}_{-27}	FASTWIND (He)	MKE06
			39.0±1.5	4.15±0.10	4.81±0.10	300	CMFGEN (He)	BLM13
			$35.5^{+3.7}_{-1.5}$	$3.31^{+0.33}_{-0.19}$	$4.80^{+0.27}_{-0.26}$	471^{+20}_{-30}	Pipeline	This work
4-049	AzV 226	O7 IIIn((f))	$35.9^{+1.3}_{-1.0}$	$3.54^{+0.13}_{-0.08}$	5.20±0.09	313^{+27}_{-23}	FASTWIND (He)	MKE06
			$33.7^{+1.5}_{-1.5}$	$3.10^{+0.16}_{-0.16}$	$5.17^{+0.25}_{-0.25}$	354^{+137}_{-26}	Pipeline	This work
2-020	AzV 83	O7 Iaf$^+$	32.8	3.25	5.54	70:	CMFGEN (He)	HLH03
			$35.7^{+1.5}_{-3.1}$	$3.31^{+0.14}_{-0.29}$	$5.61^{+0.21}_{-0.23}$	77^{+97}_{-19}	Pipeline	This work
4-058	Sk 80	O7 Iaf$^+$	$34.1^{+0.6}_{-0.6}$	$3.35^{+0.17}_{-0.12}$	$6.02^{+0.06}_{-0.06}$	74^{+15}_{-9}	FASTWIND (He)	MKE06
			33.5 ± 1.0	3.16 ± 0.10	5.89 ± 0.10	75	CMFGEN (He)	BMH21
			$35.7^{+1.5}_{-1.9}$	$3.50^{+0.14}_{-0.14}$	$6.12^{+0.15}_{-0.16}$	78^{+98}_{-19}	Pipeline	This work
1-012	AzV 267	O7.5 Vn	35.7±1.5	4.00 ± 0.20	4.90±0.10	220	CMFGEN (He)	BLM13
			$33.7^{+3.0}_{-2.7}$	$3.69^{+0.67}_{-0.48}$	$4.93^{+0.28}_{-0.28}$	303^{+29}_{-28}	Pipeline	This work
1-027	AzV 296	O7.5 V((f))n	35.0	3.5	5.30	···	CMFGEN (He)	MKB04
			$33.7^{+1.5}_{-3.0}$	$3.53^{+0.27}_{-0.54}$	$5.16^{+0.26}_{-0.27}$	354^{+134}_{-31}	Pipeline	This work
2-035	AzV 95	O7.5 III((f))	38.0±0.10	3.70±0.10	5.46±0.10	55	CMFGEN (He)	BMH21
			$35.6^{+1.5}_{-1.5}$	$3.50^{+0.14}_{-0.14}$	$5.50^{+0.21}_{-0.21}$	77^{+97}_{-20}	Pipeline	This work
7-072	AzV 251	O8 Vnn	36.0	3.90	5.01	500	CMFGEN (He)	MBH24
			$31.8^{+2.3}_{-2.3}$	$3.12^{+0.29}_{-0.29}$	$4.96^{+0.27}_{-0.27}$	413^{+25}_{-29}	Pipeline	This work
3-078	AzV 47	O8 III((f))	35.0±1.0	3.75±0.10	5.44±0.10	60	CMFGEN (He)	BMH21
			$35.6^{+1.5}_{-1.5}$	$4.36^{+0.11}_{-0.19}$	$5.56^{+0.26}_{-0.26}$	78^{+96}_{-20}	Pipeline	This work
7-001	NGC330 ELS 13	O8.5 III((f))	$34.5^{+0.8}_{-0.9}$	$3.40^{+0.14}_{-0.15}$	$5.40^{+0.07}_{-0.07}$	73^{+9}_{-11}	FASTWIND (He)	MKE06
			$33.7^{+1.1}_{-1.5}$	$3.50^{+0.14}_{-0.14}$	$5.35^{+0.24}_{-0.24}$	54^{+76}_{-16}	Pipeline	This work
4-074	NGC346 ELS 31	O9 V	$39.5^{+1.4}_{-1.2}$	$3.99^{+0.18}_{-0.24}$	$4.99^{+0.08}_{-0.08}$	18^{+10}_{-9}	FASTWIND (He)	MKE06
			37.2±1.5	4.00 ± 0.10	4.95 ± 0.10	25	CMFGEN (He)	BLM13
			$35.5^{+1.5}_{-1.5}$	$4.07^{+0.16}_{-0.22}$	$4.96^{+0.27}_{-0.27}$	0^{+25}_{-0}	Pipeline	This work
4-073	NGC346 ELS 25	O9.2 V	$36.2^{+1.2}_{-0.8}$	$4.07^{+0.24}_{-0.08}$	$4.90^{+0.08}_{-0.08}$	138^{+17}_{-14}	FASTWIND (He)	MKE06
			$35.5^{+1.9}_{-3.4}$	$4.50^{+0}_{-0.70}$	$45.02^{+0.07}_{-0.06}$	202^{+26}_{-26}	Pipeline	This work
4-026	NGC346 ELS 18	O9.5 IIIpe	$32.7^{+1.1}_{-1.3}$	$3.33^{+0.15}_{-0.14}$	5.10±0.09	138^{+38}_{-30}	FASTWIND (He)	MKE06
			$29.9^{+3.1}_{-1.2}$	$3.21^{+1.05}_{-0.24}$	$5.14^{+0.20}_{-0.18}$	353^{+42}_{-43}	Pipeline	This work
2-007	AzV 70	O9.5 II-I	28.5	3.1	5.68	100	CMFGEN (He)	ECF04
			$29.9^{+1.5}_{-1.1}$	$3.31^{+0.14}_{-0.14}$	$5.90^{+0.15}_{-0.15}$	113^{+20}_{-19}	Pipeline	This work
1-066	AzV 327	O9.7 II-Ib	30.8	3.2	5.60	150	FASTWIND (He)	MZM09
			30.0±1.0	3.12±0.10	5.54±0.10	95	CMFGEN (He)	BMH21
			$29.9^{+1.1}_{-1.1}$	$3.31^{+0.14}_{-0.14}$	$5.47^{+0.25}_{-0.25}$	55^{+77}_{-14}	Pipeline	This work

Notes. BLM13: Bouret et al. (2013); BMH21: Bouret et al. (2021); ECF04: Evans et al. (2004b); HLH03: Hillier et al. (2003); MBK04: Massey et al. (2004); MKE06: Mokiem et al. (2006); MZM09: Massey et al. (2009); MBH24: Martins et al. (2024).

Table B2. Comparison of pipeline-derived physical parameters of BLOeM B-type stars with representative literature results. Previous analyses involve FASTWIND (Puls et al. 2005; Rivero González et al. 2012), CMFGEN (Hillier & Miller 1998), or TLUSTY (Hubeny & Lanz 1995).

BLOeM	Alias	Spect. type	$T_{\rm eff}$ kK	log g cm s^{-2}	log L L$_\odot$	$v_{\rm e}\sin i$ km s^{-1}	Fitting tool	Ref.
4-013	NGC346 ELS 43	B0 V	33.0±1.0	4.25±0.20	4.71	10±5	TLUSTY (Si)	HDS07
			$31.8^{+3.0}_{-2.7}$	$4.12^{+0.33}_{-0.52}$	$4.77^{+0.26}_{-0.26}$	36^{+18}_{-21}	Pipeline	This work
4-014	NGC346 ELS 26	B0 III	31.0 ± 1.5	3.65 ± 0.10	4.93 ± 0.10	60	CMFGEN (He)	BLM13
			$32.6^{+0.4}_{-1.2}$	$3.76^{+0.05}_{-0.17}$	$4.93^{+0.09}_{-0.09}$	67^{+9}_{-5}	FASTWIND (He)	MKE06
			$31.9^{+1.2}_{-2.7}$	$3.70^{+0.17}_{-0.34}$	$4.95^{+0.21}_{-0.22}$	75^{+20}_{-23}	Pipeline	This work
2-110	AzV 148	B0 II	31.0	3.60	5.16	35	CMFGEN (He)	MBH24
			$29.9^{+1.5}_{-1.1}$	$3.50^{+0.14}_{-0.14}$	$5.12^{+0.25}_{-0.25}$	0^{+19}_{-0}	Pipeline	This work
6-080	AzV 488	B0 Ia	27.5	2.9	5.74	80	CMFGEN (Si)	ECF04
			$26.8^{+1.1}_{-1.5}$	$2.88^{+0.19}_{-0.14}$	$5.98^{+0.14}_{-0.15}$	78^{+98}_{-19}	Pipeline	This work
7-064	AzV 235	B0 Ia	27.5	2.9	5.72	80	CMFGEN (He)	ECF04
			$26.8^{+1.1}_{-1.5}$	$2.88^{+0.19}_{-0.14}$	$5.93^{+0.15}_{-0.16}$	78^{+97}_{-19}	Pipeline	This work
5-105	AzV 420	B0.7 II	27.0±1.5	3.05±0.15	5.35	80	FASTWIND (Si)	TL05
			$26.8^{+1.9}_{-1.5}$	$3.12^{+0.24}_{-0.19}$	$5.41^{+0.26}_{-0.25}$	55^{+77}_{-13}	Pipeline	This work
4-015	AzV 202	B1 II-Ib	$26.3^{+0.8}_{-0.5}$	$3.35^{+0.10}_{-0.05}$	4.80±0.08	29±4	FASTWIND (Si)	MKE06
			$23.8^{+1.1}_{-1.1}$	$3.12^{+0.14}_{-0.19}$	$4.83^{+0.24}_{-0.24}$	54^{+76}_{-15}	Pipeline	This work
4-020	AzV 210	B1 Ib-Iab	20.5±1.5	2.40±0.15	5.41	65	FASTWIND (Si)	TLP04
			$23.7^{+1.2}_{-3.1}$	$2.90^{+0.17}_{-0.34}$	$5.65^{+0.15}_{-0.20}$	55^{+77}_{-13}	Pipeline	This work
8-008	AzV 96	B1 Iab	22.0±1.5	2.55±0.15	5.39	90	FASTWIND (Si)	TL05
			$23.7^{+1.2}_{-2.7}$	$2.73^{+0.23}_{-0.29}$	$5.54^{+0.14}_{-0.18}$	78^{+98}_{-19}	Pipeline	This work
4-078	AzV 242	B1 Ia	25.0±1.5	2.85±0.15	5.67	90	FASTWIND (Si)	TL05
			$23.8^{+1.1}_{-1.1}$	$2.69^{+0.14}_{-0.14}$	$5.79^{+0.15}_{-0.15}$	78^{+98}_{-19}	Pipeline	This work
1-009	AzV 264	B1 Ia	22.5±1.5	2.55±0.15	5.44	85	FASTWIND (Si)	TL05
			$22.3^{+2.3}_{-1.9}$	$2.50^{+0.33}_{-0.14}$	$5.55^{+0.18}_{-0.17}$	78^{+98}_{-19}	Pipeline	This work
2-113	AzV 151	B2.5 Ia	16.0±1.5	2.10±0.15	5.28	62	FASTWIND (Si)	TL05
			$17.7^{+1.9}_{-1.5}$	$2.31^{+0.29}_{-0.14}$	$5.45^{+0.17}_{-0.16}$	55^{+77}_{-13}	Pipeline	This work
1-111	AzV 362	B3 Ia	14.0±1.5	1.70±0.15	5.50	51	FASTWIND (Si)	TLP04
			$14.9^{+1.5}_{-0.4}$	$1.64^{+0.38}_{-0.10}$	$5.62^{+0.17}_{-0.14}$	55^{+77}_{-13}	Pipeline	This work

Notes. BLM13: Bouret et al. (2013); ECF04: Evans et al. (2004b); HDS07: Hunter et al. (2007); MKE06: Mokiem et al. (2006); MBH24: Martins et al. (2024); TLP04: Trundle et al. (2004); TL05: Trundle & Lennon (2005).

APPENDIX C: PIPELINE VERSUS RIOTS4 RESULTS

Table C1. Comparison of pipeline-derived physical parameters for BLOeM (this work) targets in common with the RIOTS4 study of Castro et al. (2018), sorted by spectral type. [M2002] catalogue numbers (Massey 2002) used in the RIOTS4 survey are included.

BLOeM	M2002	Spect. type	$\log T_{\rm eff}/{\rm K}$ RIOTS4	$\log T_{\rm eff}/{\rm K}$ BLOeM	$\Delta \log T_{\rm eff}$	$\log L/{\rm L}_{\odot}$ RIOTS4	$\log L/{\rm L}_{\odot}$ BLOeM	$\Delta \log L/{\rm L}_{\odot}$
6-105	77368	O6 V:n	4.57±0.03	$4.58^{+0.04}_{-0.03}$	+0.01	5.31±0.18	$5.45^{+0.27}_{-0.25}$	+0.14
4-049	46035	O7 IIIn((f))	4.54±0.02	4.53±0.02	−0.01	5.04±0.21	5.17±0.25	+0.13
3-014	7782	O8 Vn	4.53±0.02	$4.53^{+0.03}_{-0.02}$	−0.00	5.08±0.31	$5.14^{+0.25}_{-0.23}$	+0.06
8-020	21877	O8 V	4.32±0.02	$4.55^{+0.04}_{-0.02}$	+0.23	5.28±0.30	$4.89^{+0.27}_{-0.26}$	−0.39
2-005	15742	O8.5 II:(n)	4.48±0.02	4.48±0.02	−0.00	5.27±0.21	5.34±0.22	+0.07
4-074	47478	O9 V	4.57±0.03	4.55±0.02	−0.02	4.71±0.18	4.96±0.27	+0.25
2-008	16230	O9 II:	4.48±0.01	4.48±0.02	−0.00	5.40±0.32	5.47±0.25	+0.07
6-025	75210	O9.2 V	4.54±0.02	4.55±0.02	+0.01	5.08±0.19	5.16±0.18	+0.08
5-044	62416	O9.5 IV	4.49±0.02	4.53±0.02	+0.04	4.96±0.32	4.95±0.26	−0.01
6-067	76371	O9.7 III	4.49±0.01	4.50±0.02	+0.01	5.11±0.19	$5.16^{+0.22}_{-0.23}$	+0.05
6-005	73913	O9.7 II-Ib(n)	4.41±0.02	4.45±0.03	+0.04	5.17±0.19	$5.31^{+0.17}_{-0.18}$	+0.14
1-002	49825	B0 IV:	4.49±0.01	$4.52^{+0.02}_{-0.04}$	+0.03	4.78±0.31	$4.86^{+0.27}_{-0.28}$	+0.08
6-035	75626	B0 IV	4.51±0.01	$4.50^{+0.03}_{-0.02}$	−0.01	4.66±0.24	$4.79^{+0.27}_{-0.26}$	+0.13
7-071	48601	B0 II: + B0	4.45±0.01	4.48±0.03	+0.03	5.15±0.25	$5.34^{+0.24}_{-0.23}$	+0.19
8-045	24096	B0.2 IV	4.48±0.02	$4.48^{+0.02}_{-0.04}$	−0.00	5.15±0.31	$4.82^{+0.26}_{-0.27}$	−0.33
6-056	76253	B0.5 III	4.48±0.02	$4.48^{+0.02}_{-0.05}$	−0.00	4.55±0.19	$4.64^{+0.27}_{-0.28}$	+0.09
3-028	8609	B0.5 II	4.45±0.01	$4.48^{+0.01}_{-0.05}$	+0.03	5.06±0.31	$5.20^{+0.18}_{-0.20}$	+0.14
8-022	22178	B0.5 II	4.18±0.03	$4.43^{+0.02}_{-0.01}$	+0.25	4.47±0.19	5.28±0.23	+0.81
6-111	77609	B0.5 Ib	4.38±0.01	4.43±0.02	+0.05	5.40±0.30	5.63±0.14	+0.23
1-069	55952	B0.7 III	4.45±0.01	4.43±0.06	−0.02	4.65±0.24	4.78±0.29	+0.13
2-047	20939	B1 Ib	4.30±0.08	4.38±0.04	+0.08	4.54±0.25	4.83±0.21	+0.29
8-008	19728	B1 Iab	4.32±0.02	$4.37^{+0.03}_{-0.05}$	+0.05	5.28±0.28	$5.50^{+0.14}_{-0.18}$	+0.22
4-090	49450	B1 II	4.40±0.03	$4.37^{+0.12}_{-0.04}$	−0.03	4.74±0.21	$4.72^{+0.36}_{-0.27}$	−0.02
7-051	46241	B1 II:e	4.18±0.09	$4.36^{+0.06}_{-0.12}$	+0.18	4.14±0.31	$4.51^{+0.22}_{-0.31}$	+0.37
5-062	62981	B1.5+early B+	4.46±0.02	$4.48^{+0.03}_{-0.13}$	+0.02	4.76±0.24	$4.78^{+0.27}_{-0.35}$	+0.02

APPENDIX D: PIPELINE RESULTS FROM BLOEM VERSUS XSHOOTU

Table D1. Comparison of pipeline-derived physical parameters of OB stars from BLOeM (FLAMES/LR02, this work) and XShootU (XShooter) data sets (Bestenlehner et al. 2025). Physical quantities shown in parentheses are not considered reliable.

BLOeM	Spectral type	$T_{\rm eff}$/kK XShootU	$T_{\rm eff}$/kK BLOeM	$\Delta T_{\rm eff}$ kK	$\log g/{\rm cm\,s^{-2}}$ XShootU	$\log g/{\rm cm\,s^{-2}}$ BLOeM	$\Delta \log g$ ${\rm cm\,s^{-2}}$	$\log L/{\rm L_\odot}$ XShootU	$\log L/{\rm L_\odot}$ BLOeM	$\Delta \log L$ ${\rm L_\odot}$	$v_{\rm e} \sin i$ XShootU	$v_{\rm e} \sin i$ BLOeM	$\Delta v_{\rm e} \sin i$ ${\rm km\,s^{-1}}$
2-016	O6 III:nn(f)p	$35.4^{+4.7}_{-1.6}$	$35.4^{+1.9}_{-3.1}$	$+0.0$	$3.31^{+0.52}_{-0.14}$	$3.30^{+0.17}_{-0.34}$	-0.01	$5.56^{+0.21}_{-0.09}$	$5.65^{+0.23}_{-0.24}$	$+0.09$	250^{+30}_{-30}	357^{+131}_{-30}	$+107$
7-069	O6.5 V	$39.9^{+1.8}_{-3.6}$	$39.7^{+2.2}_{-3.4}$	-0.2	$3.69^{+0.19}_{-0.33}$	$4.07^{+0.22}_{-0.49}$	$+0.38$	$5.49^{+0.09}_{-0.16}$	$5.57^{+0.26}_{-0.27}$	$+0.08$	113^{+20}_{-19}	75^{+20}_{-22}	-38
4-057	O6.5 Vnn	$40.1^{+3.9}_{-3.1}$	$35.5^{+3.7}_{-1.5}$	-4.6	$4.31^{+0.19}_{-0.52}$	$3.31^{+0.24}_{-0.23}$	-1.00	$4.94^{+0.16}_{-0.14}$	$4.80^{+0.27}_{-0.26}$	-0.14	250^{+30}_{-30}	471^{+20}_{-30}	$+221$
2-020	O7 Iaf^{+}	$37.7^{+1.6}_{-2.0}$	$35.7^{+1.5}_{-3.1}$	-2.0	$(4.07^{+0.38}_{-0.29})$	$3.31^{+0.14}_{-0.29}$	(-0.76)	$5.68^{+0.09}_{-0.10}$	$5.61^{+0.21}_{-0.23}$	-0.07	0^{+19}_{0}	77^{+97}_{-19}	$+77$
4-058	O7 Iaf^{+}	$37.7^{+1.6}_{-2.0}$	$35.7^{+1.5}_{-1.9}$	-2.0	$3.69^{+0.24}_{-0.14}$	$3.50^{+0.14}_{-0.14}$	-0.19	$6.17^{+0.09}_{-0.10}$	$6.12^{+0.15}_{-0.16}$	-0.05	54^{+74}_{-18}	78^{+98}_{-18}	$+24$
1-012	O7.5 Vn	$35.4^{+3.1}_{-1.6}$	$33.7^{+3.0}_{-2.7}$	-1.7	$3.69^{+0.52}_{-0.19}$	$3.69^{+0.67}_{-0.48}$	$+0.00$	$4.89^{+0.15}_{-0.09}$	$4.93^{+0.28}_{-0.28}$	$+0.04$	250^{+30}_{-30}	303^{+28}_{-28}	$+53$
1-027	O7.5 V((f))n	$33.4^{+5.1}_{-3.3}$	$33.7^{+1.5}_{-3.0}$	$+0.2$	$3.31^{+0.81}_{-0.35}$	$3.53^{+0.27}_{-0.54}$	$+0.22$	$5.06^{+0.23}_{-0.16}$	$5.16^{+0.26}_{-0.27}$	$+0.10$	251^{+30}_{-29}	354^{+134}_{-31}	$+103$
2-035	O7.5 III((f))	$37.7^{+3.1}_{-2.0}$	$35.6^{+1.5}_{-1.5}$	-2.1	$3.69^{+0.29}_{-0.14}$	$3.50^{+0.14}_{-0.14}$	$+0.19$	$5.56^{+0.14}_{-0.10}$	$5.50^{+0.21}_{-0.21}$	-0.06	53^{+77}_{-17}	77^{+97}_{-19}	$+24$
3-078	O8 III((f))	$35.4^{+1.6}_{-1.2}$	$35.6^{+1.5}_{-1.5}$	$+0.2$	$3.69^{+0.14}_{-0.14}$	$4.36^{+0.10}_{-0.19}$	$+0.67$	$5.46^{+0.09}_{-0.08}$	$5.56^{+0.26}_{-0.26}$	$+0.10$	113^{+20}_{-19}	78^{+96}_{-20}	-35
5-097	O8 II(f)	$35.4^{+2.0}_{-1.6}$	$37.5^{+1.9}_{-1.5}$	$+2.1$	$3.69^{+0.14}_{-0.14}$	$4.31^{+0.14}_{-0.24}$	$+0.62$	$4.77^{+0.11}_{-0.09}$	$4.94^{+0.27}_{-0.27}$	$+0.17$	33^{+14}_{-20}	22^{+10}_{-22}	-11
7-001	O8.5 III((f))	$33.4^{+1.6}_{-1.6}$	$33.7^{+1.1}_{-1.5}$	$+0.3$	$3.31^{+0.14}_{-0.14}$	$3.50^{+0.14}_{-0.14}$	$+0.19$	$5.27^{+0.09}_{-0.09}$	$5.35^{+0.24}_{-0.24}$	$+0.08$	78^{+98}_{-19}	78^{+19}_{-20}	0
4-074	O9 V	$35.4^{+3.5}_{-1.6}$	$35.5^{+1.5}_{-1.5}$	$+0.1$	$3.69^{+0.33}_{-0.14}$	$4.07^{+0.16}_{-0.22}$	$+0.38$	$4.86^{+0.16}_{-0.09}$	$4.96^{+0.27}_{-0.27}$	$+0.10$	0^{+18}_{0}	0^{+25}_{0}	$+0$
4-073	O9.2 V	$35.4^{+1.6}_{-2.3}$	$35.5^{+1.9}_{-3.4}$	$+0.1$	$4.12^{+0.14}_{-0.48}$	$4.50^{+0}_{-0.70}$	$+0.38$	$4.92^{+0.09}_{-0.12}$	$5.02^{+0.27}_{-0.28}$	$+0.10$	153^{+24}_{-24}	153^{+24}_{-24}	$+0$
2-007	O9.5 II-I	$28.3^{+1.2}_{-1.2}$	$29.9^{+1.5}_{-1.1}$	$+1.6$	$2.88^{+0.19}_{-0.14}$	$3.31^{+0.14}_{-0.14}$	$+0.43$	$5.66^{+0.09}_{-0.09}$	$5.90^{+0.15}_{-0.15}$	$+0.24$	79^{+93}_{-20}	113^{+20}_{-19}	$+34$
1-056	O9.5 Ibn	$29.9^{+3.1}_{-2.0}$	$28.4^{+1.1}_{-1.5}$	-1.5	$3.12^{+0.33}_{-0.29}$	$2.88^{+0.19}_{-0.14}$	-0.24	$5.14^{+0.17}_{-0.12}$	$5.16^{+0.26}_{-0.26}$	$+0.02$	249^{+30}_{-30}	301^{+28}_{-27}	$+52$
4-076	O9.7 III	$33.4^{+1.6}_{-1.2}$	$31.8^{+1.5}_{-1.5}$	-1.6	$3.69^{+0.14}_{-0.14}$	$3.50^{+0.14}_{-0.14}$	-0.19	$5.36^{+0.09}_{-0.08}$	$5.36^{+0.26}_{-0.26}$	$+0.00$	55^{+77}_{-14}	55^{+76}_{-14}	$+0$
1-066	O9.7 II-Ib	$29.9^{+1.2}_{-1.2}$	$29.9^{+1.1}_{-1.1}$	$+0.0$	$3.31^{+0.14}_{-0.14}$	$3.31^{+0.14}_{-0.14}$	$+0.00$	$5.40^{+0.08}_{-0.08}$	$5.47^{+0.25}_{-0.25}$	$+0.07$	55^{+76}_{-14}	55^{+77}_{-14}	$+0$
4-013	B0 V	$31.9^{+1.2}_{-1.6}$	$31.8^{+3.0}_{-2.7}$	-0.1	$4.12^{+0.14}_{-0.19}$	$4.12^{+0.33}_{-0.52}$	$+0.00$	$4.70^{+0.08}_{-0.10}$	$4.77^{+0.26}_{-0.26}$	$+0.07$	19^{+12}_{-19}	36^{+18}_{-21}	$+17$
4-014	B0 III	$31.5^{+1.6}_{-2.3}$	$31.9^{+1.2}_{-2.7}$	$+0.4$	$3.69^{+0.14}_{-0.29}$	$3.70^{+0.17}_{-0.34}$	$+0.01$	$4.93^{+0.10}_{-0.13}$	$4.95^{+0.21}_{-0.22}$	$+0.02$	55^{+77}_{-14}	75^{+20}_{-23}	$+20$
2-110	B0 II	$29.9^{+1.2}_{-1.2}$	$29.9^{+1.5}_{-1.1}$	$+0.0$	$3.50^{+0.14}_{-0.14}$	$3.50^{+0.14}_{-0.14}$	$+0.00$	$5.04^{+0.08}_{-0.08}$	$5.12^{+0.25}_{-0.25}$	$+0.08$	5^{+14}_{-5}	0^{+19}_{-0}	-5
6-080	B0 Ia	$25.2^{+1.2}_{-1.2}$	$26.8^{+1.1}_{-1.5}$	$+1.6$	$2.69^{+0.14}_{-0.14}$	$2.88^{+0.19}_{-0.14}$	$+0.19$	$5.79^{+0.09}_{-0.09}$	$5.98^{+0.14}_{-0.15}$	$+0.19$	56^{+75}_{-14}	78^{+98}_{-18}	$+22$
7-064	B0 Ia	$28.3^{+1.2}_{-1.6}$	$26.8^{+1.1}_{-1.5}$	-1.5	$(3.50^{+0.24}_{-0.14})$	$2.88^{+0.19}_{-0.14}$	(-0.62)	$6.01^{+0.09}_{-0.11}$	$5.93^{+0.15}_{-0.16}$	-0.08	31^{+14}_{-20}	78^{+97}_{-19}	$+47$
4-020	B1 Ib-Iab	$23.7^{+1.2}_{-2.0}$	$23.7^{+1.2}_{-3.1}$	$+0.0$	$2.69^{+0.14}_{-0.29}$	$2.90^{+0.17}_{-0.34}$	$+0.21$	$5.56^{+0.10}_{-0.14}$	$5.65^{+0.15}_{-0.20}$	$+0.09$	55^{+76}_{-13}	55^{+77}_{-13}	$+0$
8-008	B1 Iab	$21.3^{+1.6}_{-1.2}$	$23.7^{+1.2}_{-2.7}$	$+2.4$	$2.31^{+0.29}_{-0.19}$	$2.73^{+0.23}_{-0.29}$	$+0.42$	$5.23^{+0.13}_{-0.11}$	$5.54^{+0.13}_{-0.18}$	$+0.31$	78^{+98}_{-19}	78^{+98}_{-19}	$+0$
4-045	B1 Iab	$23.7^{+1.2}_{-2.0}$	$23.7^{+2.2}_{-3.0}$	$+0.0$	$3.12^{+0.14}_{-0.33}$	$2.88^{+0.33}_{-0.29}$	-0.24	$4.83^{+0.10}_{-0.14}$	$4.88^{+0.25}_{-0.27}$	$+0.05$	113^{+20}_{-19}	201^{+24}_{-24}	$+88$
4-078	B1 Ia	$22.5^{+0.8}_{-0.8}$	$23.8^{+1.1}_{-1.1}$	$+1.3$	$2.31^{+0.14}_{-0.14}$	$2.69^{+0.14}_{-0.14}$	$+0.38$	$5.28^{+0.08}_{-0.08}$	$5.79^{+0.15}_{-0.15}$	$+0.51$	112^{+20}_{-19}	78^{+98}_{-19}	–34
1-009	B1 Ia	$21.3^{+0.8}_{-1.2}$	$22.3^{+2.3}_{-1.9}$	$+1.0$	$2.31^{+0.14}_{-0.14}$	$2.49^{+0.12}_{-0.11}$	$+0.18$	$5.30^{+0.08}_{-0.11}$	$5.55^{+0.18}_{-0.17}$	$+0.25$	78^{+98}_{-19}	78^{+97}_{-19}	$+0$
4-066	B2.5 Ib	$17.8^{+0.8}_{-0.8}$	$18.8^{+0.8}_{-1.5}$	$+1.0$	$2.50^{+0.14}_{-0.14}$	$2.69^{+0.14}_{-0.33}$	$+0.19$	$5.06^{+0.09}_{-0.09}$	$5.16^{+0.18}_{-0.20}$	$+0.10$	36^{137}_{-34}	36^{+56}_{-34}	$+0$
1-111	B3 Ia	$15.9^{+0.8}_{-0.8}$	$14.9^{+1.5}_{-0.4}$	-1.0	$1.64^{+0.19}_{-0.10}$	$1.64^{+0.38}_{-0.10}$	$+0.00$	$4.86^{+0.10}_{-0.10}$	$5.62^{+0.17}_{-0.14}$	$+0.76$	5^{+8}_{-5}	55^{+77}_{-13}	$+50$
1-062	B8 Iab	$12.7^{+0.4}_{-0.4}$	$13.5^{+0.4}_{-0.8}$	$+0.8$	$1.88^{+0.19}_{-0.33}$	$2.10^{+0.17}_{-0.17}$	$+0.22$	$4.65^{+0.07}_{-0.07}$	$4.77^{+0.16}_{-0.17}$	$+0.12$	55^{+77}_{-13}	35^{+57}_{-32}	–20

APPENDIX E: HR DIAGRAMS OF SINGLE AND BINARY SYSTEMS

Fig. E1 shows HR diagrams of single (upper) and binary (lower) BLOeM OB stars, colour coded by luminosity class, together with Brott et al. (2011) non-rotating SMC tracks. Fig. E2 shows HR diagrams for single (upper) and binary (lower) BLOeM OB stars, colour coded by $v_e \sin i$, together with Schootemeijer et al. (2019) non-rotating SMC tracks.

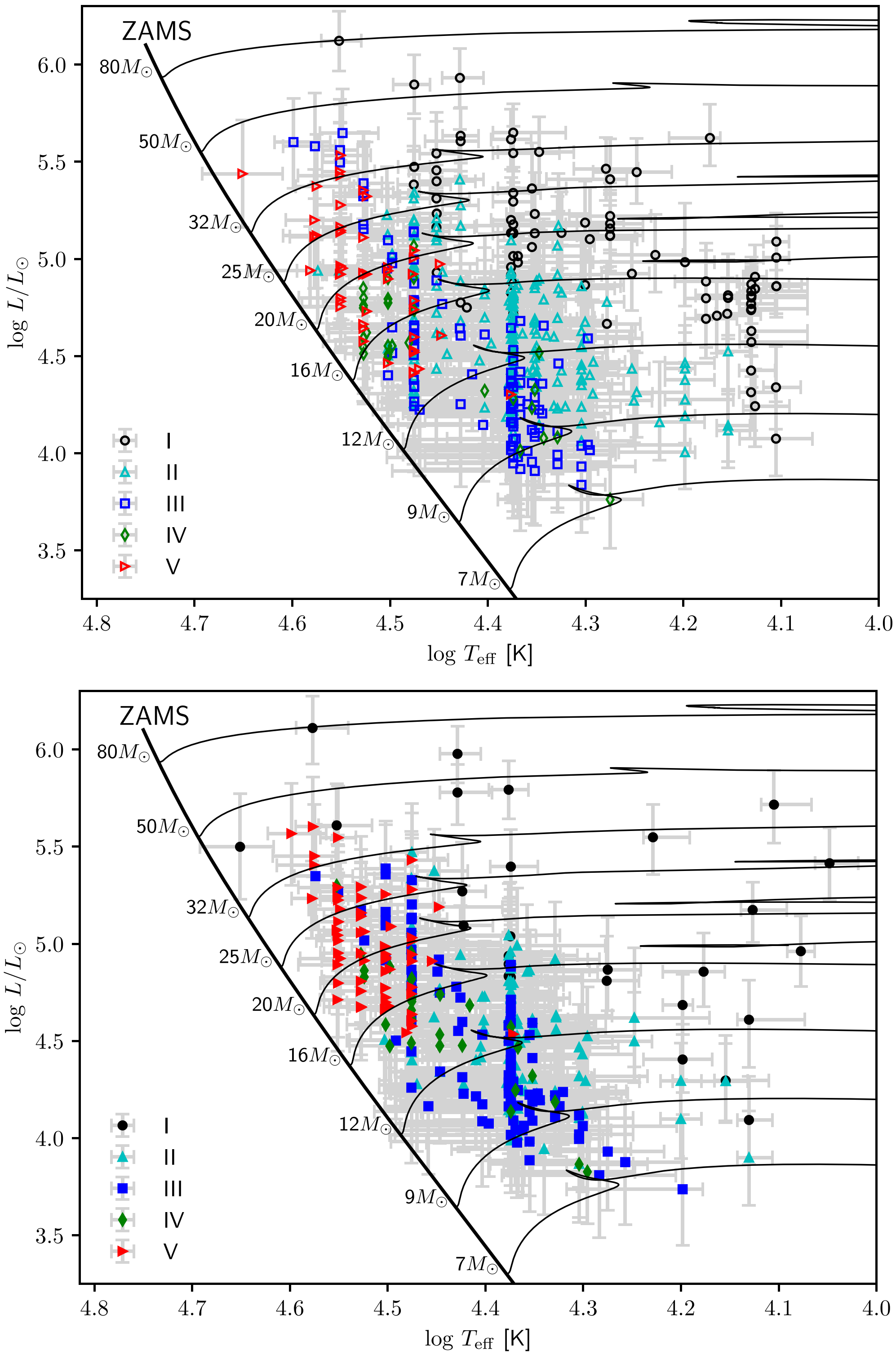

Figure E1. HR diagram of single (upper panel) and multiple (lower panel) OB stars (colour coded by luminosity class) on the basis of the initial nine BLOeM epochs, together with evolutionary tracks for non-rotating SMC massive stars from Brott et al. (2011), with the exception of two luminous O supergiants drawn from Hastings et al. (2021).

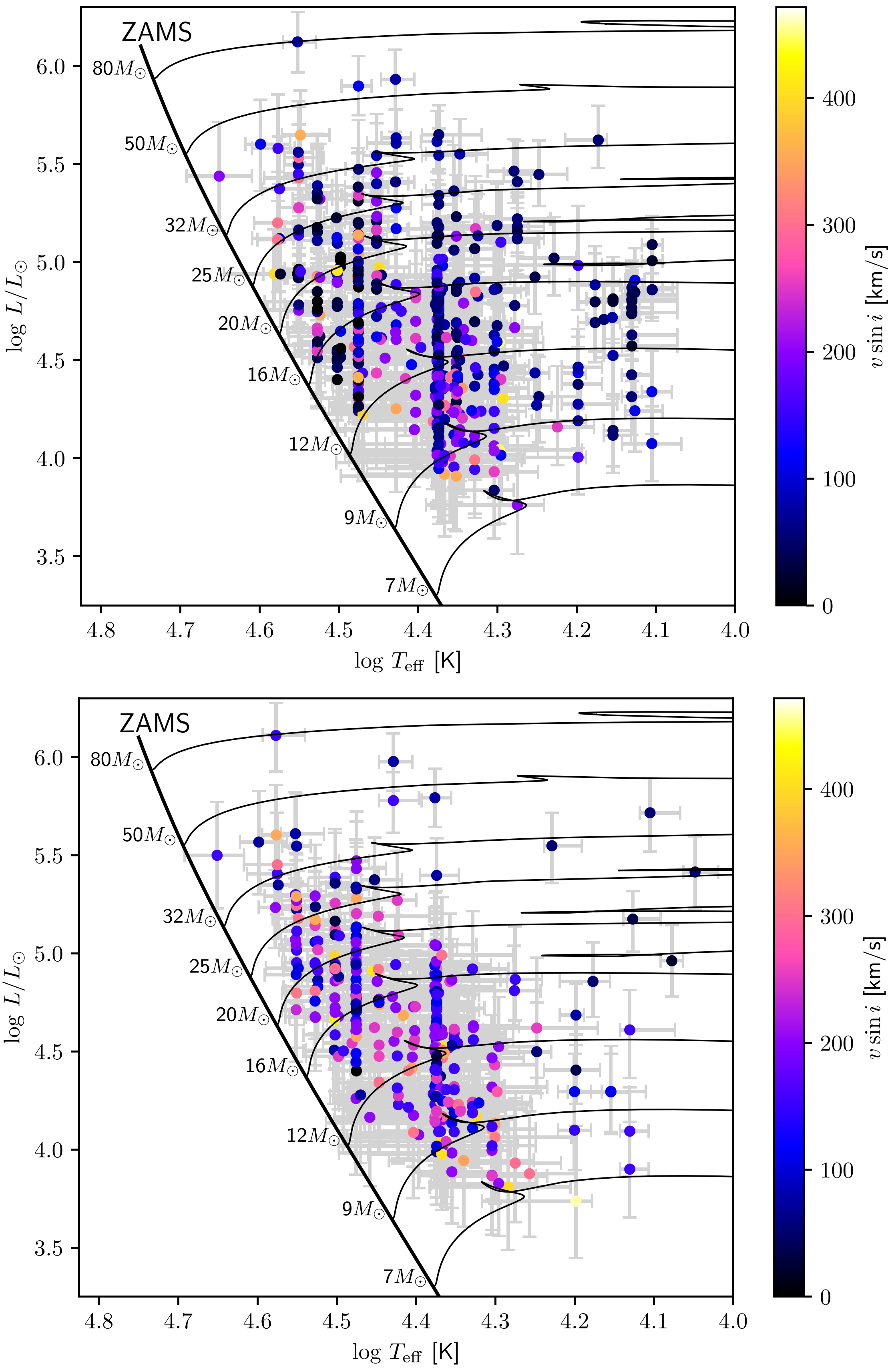

Figure E2. HR diagram of OB stars (colour coded by $v_e \sin i$) for single (upper panel) and multiple (lower panel) systems on the basis of the initial nine BLOeM epochs, together with evolutionary tracks for SMC massive stars from Schootemeijer et al. (2019) for non-rotating stars ($\alpha_{\rm SC} = 10$, $\alpha_{\rm OV} = 0.33$).

APPENDIX F: INDIVIDUAL RESULTS FROM IACOB-BROAD AND IACOB-GBAT

Table F1. Physical parameters for subset of BLOeM OB stars obtained with IACOB-BROAD (Simón-Díaz & Herrero 2014) and IACOB-GBAT (Simón-Díaz et al. 2011). Rotation velocities are obtained via FT or GOF for He I λ4387. Helium abundances are provided by number, y = N(He)/N(H) and by mass, Y where $y = 0.085$ ($Y = 0.25$) is the baseline He content in the SMC adopted by Brott et al. (2011).

BLOeM	Spect. type	$T_{\rm eff}$ kK	$\log g$ cm s^{-2}	$v_{\rm e} \sin i$ (km s^{-1}) FT	GOF	$y \times 10^2$	Y	Note
1-010	B1.5 III:	–	–	158	110^{+63}_{-96}	–	–	
1-020	B0 III	30.8 ± 1.2	3.75 ± 0.18	77	70^{+28}_{-36}	$<6.0^{+2.0}$	$<0.19^{+0.05}$	SB1
1-030	B1 II	–	–	80	81^{+77}_{-67}	–	–	
1-060	B1.5 Ib	–	–	191	190^{+19}_{-30}	–	–	
1-070	B1.5 II	–	–	57	57^{+19}_{-24}	–	–	
1-080	O8:V:+B + B	34.5 ± 1.3	$>4.30_{-0.28}$	86	63^{+86}_{-49}	$<6.0^{+1.3}$	$<0.19^{+0.03}$	
1-100	B1 II	–	–	98	79^{+19}_{-23}	–	–	SB1
1-110	B1 Ib	–	–	57	21^{+15}_{-7}	–	–	
2-010	B1.5 III-II	–	–	47	14^{+36}_{-0}	–	–	
2-020	O7 Iaf^{+}	37.6 ± 1.5	3.58 ± 0.17	77	78^{+30}_{-64}	10.2 ± 2.9	$0.29^{+0.05}_{-0.07}$	SB1
2-030	B2 II	–	–	169	148^{+130}_{-135}	–	–	lpv/SB1
2-040	B2 II	–	–	53	28^{+23}_{-15}	–	–	
2-060	B1.5 Ib	–	–	74	64^{+21}_{-26}	–	–	
2-070	B1 II e	–	–	104	90^{+29}_{-38}	–	–	SB?
2-090	O7.5 Vn	35.8 ± 1.4	3.99 ± 0.24	309	276^{+151}_{-228}	$<6.0^{+3.2}$	$<0.19^{+0.08}$	SB2
2-100	B0 V	32.7 ± 0.8	4.10 ± 0.11	145	130^{+34}_{-54}	7.7 ± 1.0	$0.23^{+0.03}_{-0.02}$	
2-110	B0 II	31.3 ± 0.9	3.59 ± 0.13	44	14^{+19}_{-0}	8.6 ± 2.2	$0.25^{+0.05}_{-0.05}$	
3-010	O9.7 V:	35.4 ± 1.0	$>4.50_{-0.32}$	80	64^{+83}_{-51}	$<6.0^{+1.0}$	$<0.19^{+0.03}$	SB1
3-020	B0 III	31.0 ± 1.2	3.91 ± 0.13	72	28^{+48}_{-14}	$<6.0^{+2.3}$	$<0.19^{+0.06}$	SB2
3-030	B1 II	–	–	128	120^{+17}_{-24}	–	–	
3-050	B1.5 III	–	–	173	132^{+53}_{-60}	–	–	SB1
3-060	O6 Vn:	37.7 ± 1.1	3.62 ± 0.16	294	285^{+118}_{-271}	12.5 ± 3.1	$0.33^{+0.05}_{-0.06}$	
3-070	B1 II	–	–	38	14^{+10}_{-0}	–	–	SB1
3-080	B1 III-II	–	–	59	14^{+20}_{-0}	–	–	SB1
3-090	B0.2 Ia	28.0 ± 1.1	3.19 ± 0.21	75	43^{+12}_{-17}	$<6.0^{+2.3}$	$<0.19^{+0.06}$	
3-100	B3 II	–	–	61	50^{+32}_{-37}	–	–	
3-110	B8 II-Ib	–	–	46	14^{+38}_{-0}	–	–	Post-MS
4-020	B1 Iab-Ib	–	–	62	31^{+19}_{-18}	–	–	
4-030	B1 Ia	–	–	58	37^{+13}_{-18}	–	–	lpv/SB1
4-050	B1 II:	–	–	55	14^{+42}_{-0}	–	–	
4-060	B8 II-Ib	–	–	60	14^{+44}_{-0}	–	–	Post-MS
4-070	B2 II	–	–	301	305^{+54}_{-218}	–	–	lpv/SB1
4-080	O9.7+O8-8.5 + B	–	–	227	21^{+151}_{-7}	–	–	SB2
4-090	B1 II	–	–	134	116^{+26}_{-30}	–	–	SB1
4-100	B1 III	–	–	73	28^{+37}_{-14}	–	–	
4-110	O7 V:(n)	35.8 ± 1.5	3.90 ± 0.28	228	104^{+206}_{-91}	$<6.0^{+2.3}$	$<0.19^{+0.06}$	SB1
5-010	B3 II	–	–	44	14^{+26}_{-0}	–	–	
5-030	B1.5 III:	–	–	107	108^{+59}_{-80}	–	–	SB2
5-040	B1 II	–	–	66	16^{+30}_{-2}	–	–	SB1
5-050	O9.7 V: + early B	32.0 ± 0.4	3.74 ± 0.08	317	307^{+24}_{-32}	8.9 ± 1.5	$0.26^{+0.03}_{-0.03}$	SB2
5-060	B1.5 II	–	–	43	14^{+15}_{-0}	–	–	
5-070	B2 III:	–	–	293	260^{+123}_{-222}	–	–	
5-080	B2 III:	–	–	344	344^{+42}_{-87}	–	–	SB2

Table F1 – *continued*

BLOeM	Spect. type	$T_{\rm eff}$ kK	$\log g$ cm s^{-2}	$v_{\rm e} \sin i$ (km s^{-1}) FT	GOF	$y \times 10^2$	Y	Note
5-090	O9.5 III	34.4 ± 0.6	3.64 ± 0.06	86	66^{+20}_{-24}	16.0 ± 3.9	$0.39^{+0.05}_{-0.07}$	
5-100	B0 V	31.9 ± 1.3	4.10 ± 0.21	122	122^{+59}_{-78}	$<6.0^{+1.8}$	$<0.19^{+0.05}$	SB2
5-110	B1 III	–	–	107	75^{+63}_{-61}	–	–	SB2
6-010	B2 IV:	–	–	133	52^{+212}_{-39}	–	–	SB2
6-020	B2.5 III	–	–	139	142^{+33}_{-44}	–	–	SB1
6-030	B0 IV:	32.9 ± 1.6	4.02 ± 0.23	41	14^{+38}_{-0}	$<8.0^{+2.1}$	$<0.24^{+0.05}$	
6-040	B1.5 III:	–	–	109	104^{+54}_{-91}	–	–	
6-050	B1 III	–	–	49	14^{+22}_{-0}	–	–	
6-060	O9.7 IV	35.0 ± 1.1	4.11 ± 0.16	47	14^{+30}_{-0}	8.8 ± 1.9	$0.26^{+0.04}_{-0.04}$	
6-070	B1: II	–	–	123	121^{+39}_{-49}	–	–	SB1
6-080	B0 Ia	29.0 ± 1.6	3.43 ± 0.28	56	55^{+10}_{-7}	$<8.0^{+1.6}$	$<0.24^{+0.04}$	lpv/SB1
6-090	B2 III	–	–	358	365^{+112}_{-352}	–	–	
6-100	B1 II	–	–	35	14^{+14}_{-0}	–	–	
6-110	B1.5 III:	–	–	34	14^{+20}_{-0}	–	–	
7-010	B1 III	–	–	56	14^{+27}_{-0}	–	–	SB1
7-030	B0.5: V	30.9 ± 2.4	$>4.10_{-0.28}$	101	87^{+97}_{-73}	$<6.0^{+3.1}$	$<0.19^{+0.08}$	
7-040	B1.5 III-II	–	–	108	101^{+31}_{-46}	–	–	SB1
7-050	B2 III:	–	–	201	173^{+82}_{-159}	–	–	
7-060	B2 III:	–	–	180	208^{+54}_{-84}	–	–	SB2
7-070	B1.5 III:	–	–	117	93^{+77}_{-79}	–	–	SB1
7-080	B1.5 III:	–	–	119	96^{+57}_{-82}	–	–	
7-090	B2 III:	–	–	162	112^{+72}_{-98}	–	–	
7-100	B2 II	–	–	114	111^{+61}_{-97}	–	–	SB1
7-110	B1.5 III:	–	–	157	134^{+65}_{-121}	–	–	SB1
8-020	O8 V	39.3 ± 1.3	$>4.30_{-0.20}$	73	63^{+74}_{-49}	$8.0^{<+1.2}$	$<0.24^{+0.03}$	SB1
8-030	O6.5 Vn	38.2 ± 0.8	3.82 ± 0.08	290	293^{+50}_{-122}	13.0 ± 2.3	$0.34^{+0.04}_{-0.04}$	
8-040	B2 IV	–	–	95	58^{+67}_{-45}	–	–	
8-050	O9.7 IV	35.7 ± 1.3	4.11 ± 0.19	42	14^{+35}_{-0}	$<8.0^{+2.2}$	$0.24^{+0.05}_{-0.04}$	
8-060	B2 II:	–	–	115	90^{+52}_{-76}	–	–	
8-070	B0.5 IV	30.0 ± 2.0	$>4.20_{-0.33}$	149	126^{+55}_{-92}	$<8.0^{+2.3}$	$0.24^{+0.05}_{-0.04}$	SB1
8-080	B2 III:	–	–	267	253^{+79}_{-187}	–	–	SB2
8-090	B1 II	–	–	114	137^{+41}_{-62}	–	–	SB1
8-100	B2 II e	–	–	245	238^{+40}_{-94}	–	–	
8-110	B1 III: + B1 III:	–	–	—	–	–	–	SB2

APPENDIX G: SPECTROSCOPIC VERSUS EVOLUTIONARY MODELS

Fig. G1 compares spectroscopic and (current) evolutionary masses of OB stars from the BLOeM survey (filled symbols are known binaries) based on Schootemeijer et al. (2019) non-rotating SMC metallicity models, which reveals a similar discrepancy to Fig. 19 based on Brott et al. (2011) rotating SMC metallicity models.

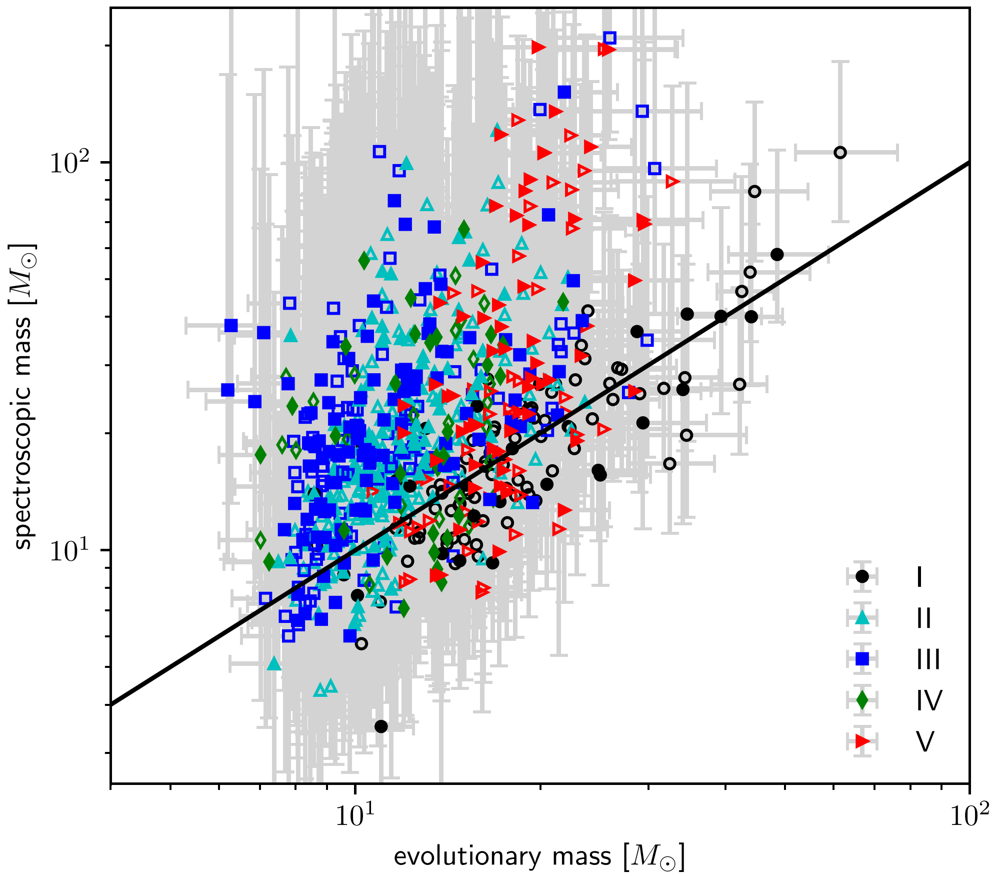

Figure G1. Comparison between (current) evolutionary masses and spectroscopic masses of BLOeM OB stars, based on Schootemeijer et al. (2019) non-rotating models, colour coded by luminosity class (filled symbols are binaries).

APPENDIX H: UPDATED CATALOGUE OF SMC O STARS

Table H1 is available in supplementary data and in electronic form at http://cdsweb.u-strasbg.fr/cgi-bin/qcat?J/A+A/.

This paper has been typeset from a TEX/LATEX file prepared by the author.